Authors' Response to Comments from anonymous referee #1

Black, italic: Referee's comments

Blue: Author's reply

Red: Changes in the original discussion paper

This manuscript the first measurements from an airborne instrument, UVHIS, which measures backscattered light in the UV and visible parts of the electromagnetic spectrum. It includes instrument characteristics and background, data processing/calibration steps, and results from a NO2 VCD retrieval from its research flight near Feicheng, China. This paper fits the scope of AMT and would be a welcome read to the AMT audience for a new capability for high spatial resolution trace gas observations in a new region of the world. However, before publishing, this manuscript requires the addressing of technical corrections that cause some concern, expansion of details in places, and some improvement on the quality of the writing. While most the comments are minor and related to the writing, I do recommend revisions in the major category because of the concern about the VCD measurement (which may be correct but needs more details to describe to convince the reader) and a great expansion of the mobile DOAS description. Detailed comments on those are below.

First, we appreciate the overall positive response of the referee and we would like to thank for his constructive comments and helpful suggestions on the manuscript. As described below, we have modified the manuscript according to suggestions and provided clarifications where necessary.

1. There are concerns about the actual calculation of the NO2 VCD as described in Sect 4.3. It is hard to tell what the VCD actually represents in the calculation. Is it a total column VCD? If so, the stratospheric details are missed. However, as it is stated that the stratospheric column is assumed stable during the flight from the reference and is canceled out leads the reader to believe it is not a total column. If it's just the below aircraft column, please state this and ensure the proper accounting for the distinction in the AMF and VCD calculation (e.g., Lamsal et al., 2017 is a great example that shows the breakdown of how these components are calculated).

In this manuscript, the NO_2 vertical columns we calculated are tropospheric vertical columns. We added necessary clarification throughout the manuscript. For example, we changed the title of the manuscript to 'The first high-resolution tropospheric NO2 observations from the Ultraviolet Visible Hyperspectral Imaing Spectrometer (UVHIS)'.

2. Line 157-158: Pertaining to the spatial and temporal variability of the stratosphere being stable. This is maybe close to correct for a 3 hours flight, however there are changes in the SZA which will impact the slant column difference between the measurement and the reference. This could be estimated with a geometric calculation of the slant path with an assumed stratospheric amount between the reference and the measurement. It likely is small.

According to TROPOMI L2 NO_2 product on 23 June, 2018, the NO_2 stratospheric vertical columns is about 3.5×10^{15} molec cm^{-2} in flight area. The SZA of reference spectra is about 13°, while the largest SZA of 37° occurred in the end of 3 hour flight. Under simple geometric approximation of light path, the largest difference of SCD of stratospheric NO_2 between the measurement and the reference is about 8×10^{14} molec cm^{-2}.

3. Lines 306 and 288: The mean slant column fitting error of 4.8x1015 molecules cm-2 and mean total value of error of 2.6x1015 molecules cm-2 for the VCD column with a range going down to 1x1015 molecules cm-2 does not seem to work out mathematically unless the AMF error is zero (which it is not) and the AMF must be ~2 (which is seems to be below that for most cases) and the error of the reference itself is 100% which is stated as 1x1015. Please check this math.

We recalculated the NO_2 dSCD by adding a H_2O vapor cross section from HITRAN database, the mean slant column fitting error slightly decreased (still about 4.8×10^{15} molec cm^{-2}). We modified the tropospheric NO_2 vertical column of reference spectra to 3×10^{15} molec cm^{-2} with error of 1×10^{15} molec cm^{-2} based on TROPOMI NO_2 product. We checked the AMF calculation, and the mean value of AMF during the flight is about 2. We also update the figure of time series of AMF, surface reflectance, SZA and RAA. After the recalculation, the mean total value of error is 3.0×10^{15} molec cm^{-2} with a range from 1.5 to 5.9×10^{15} molec cm^{-2}.

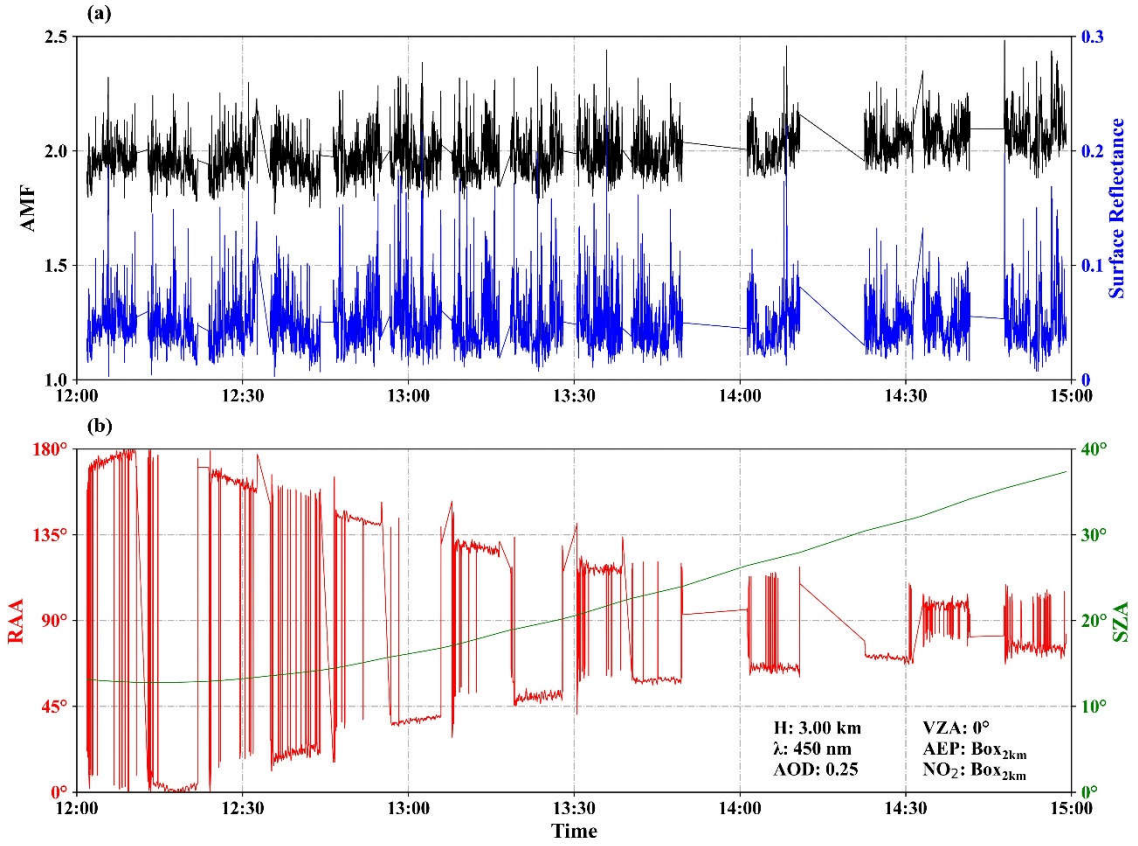

Figure 7. Time series of NO_2 AMF compared with **(a)** surface reflectance; **(b)** SZA and RAA for the research flight on 23 June 2018, computed with SCIATRAN model based on the RTM parameters from the UVHIS instrument. Only data of the nadir observations in each flight line are plotted.

4. Line 17: the error of 2.6 x1015 is not the fitting error as stated. It is the error based on all sources of uncertainty.

Corrected.

Measurements of nadir backscattered solar radiation of channel 3 are used to retrieve tropospheric vertical column densities (VCDs) of NO_2 with a mean total error of 3.0×10^{15} molec cm^{-2}.

5. Are there literature references for the mobile-DOAS measurements? If not, then details on the specifics of that measurement need to be greatly expanded upon as well as the zenith-sky NO2 retrieval in Sect 6.2. Especially details on the uncertainty and what the VCD represented vertically (just the troposphere? Stratosphere?).

We added two paragraphs in Sect 6.2 to describe the mobile DOAS tropospheric NO_2 retrieval method and its uncertainty analysis. For better comparison with UVHIS NO_2 observations, assumptions and parameters in NO_2 retrieval method for the mobile DOAS were set to the same as the UVHIS.

For better comparison with UVHIS NO_2 observations, assumptions and parameters in NO_2 retrieval method for the mobile DOAS were set to the same as the UVHIS. For example, residual amount of NO_2 in reference spectra was set to 3×10^{15} molec cm^{-2} with an error of 1×10^{15} molec cm^{-2}; mobile DOAS observations only focus on tropospheric portion of NO_2 columns, assumed that the difference of the stratospheric NO_2 columns between observed spectra and reference spectra is negligible; vertical profiles of NO_2 and aerosol extinction, albedo, and aerosol properties in the AMF calculation were set to the same as UVHIS.

Like the uncertainty analysis of UVHIS NO_2 columns, the total uncertainty on the retrieved mobile tropospheric VCD is composed of three parts: (1) the mean uncertainty on dSCD of mobile DOAS is 1.4×10^{15} molec cm^{-2}; (2) the uncertainty of reference vertical column is estimated to be 1×10^{15} molec cm^{-2}. In the case that the tropospheric AMFs of measured and reference spectra are very close, this part results an uncertainty 1×10^{15} molec cm^{-2} to the total uncertainty; (3) the mean relative uncertainty on the AMF calculation is 22 % by square root of the quadratic sum of individual uncertainties like UVHIS. Combining these uncertainties together, the mean total uncertainties on the retrieved tropospheric NO_2 VCD is 2.1×10^{15} molec cm^{-2}.

6. In Figure 2, there are lines that are repeated in the northern half of the raster. Can this be described? Does this impact the comparisons to the mobile DOAS measurements? Please describe this overlap in the paper is this is what is shown in the NO2 data. The details should be discussed in the paper.

Indeed, several fight lines are repeated in the northern part of flight area, but the spectral data of UVHIS are not recorded because of misoperation. Only spectral data of the flight lines over the steel factory are recorded, and the pass time of aircraft is 13:26 and 14:57 respectively. We added a paragraph and a figure to discuss this in detail. For impact on the comparison with mobile DOAS, see answer in question No. 22.

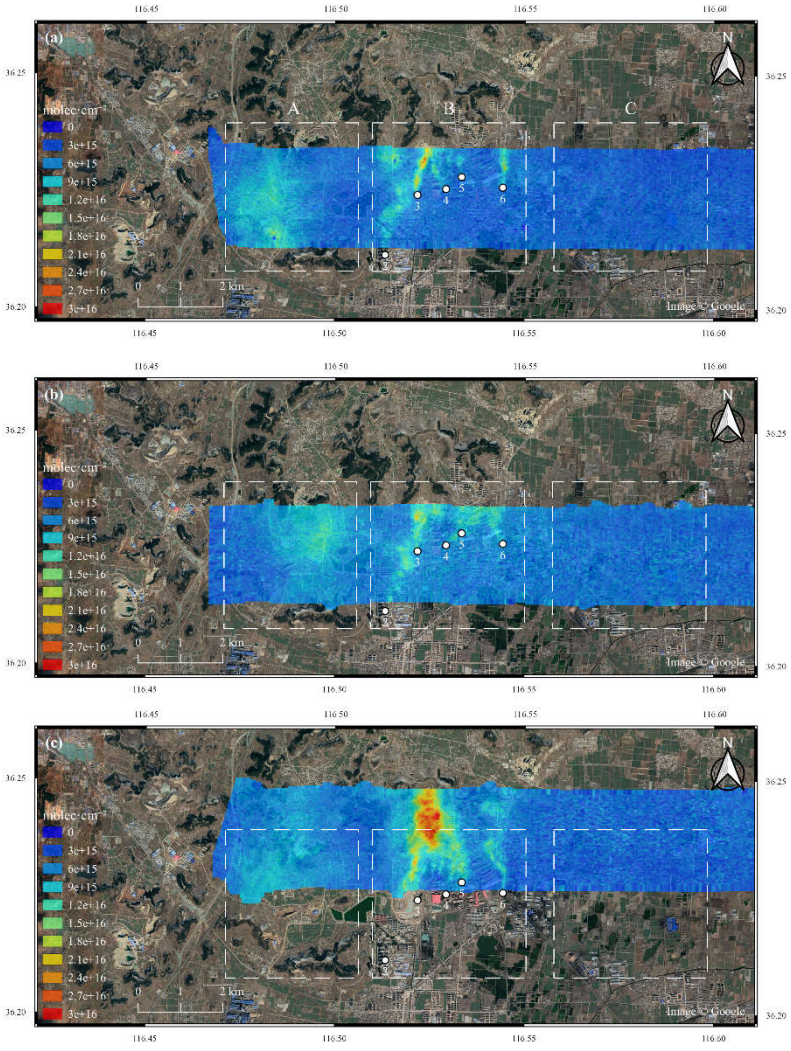

Figure 12. Three flight lines that pass through the steel factory, at local time 13:26 (a), 13:32 (c), and 14:57 (b). Panel (a) and (b) represent flight lines that cover the same area with a 1.5 hour time gap, panel (a) and (c) represent adjacent flight lines with a 6 minutes time gap.

Due to temporal discontinuity of flight lines and dynamic characteristics of NO_2 field, artefacts can be observed between adjacent flight lines. Figure 12 shows three flight lines that pass through the steel factory, at local time 13:26 (a), 13:32 (c), and 14:57 (b). Panel (a) and (b) represent flight lines that cover the same area with a 1.5 hour time gap, panel (a) and (c) represent adjacent flight lines with a 6 minutes time gap. These flight lines can be divided into three regions: region A covers no NO_2 source but is affected by carbon factories about 3 km away; region B covers the steel factory as dominant NO_2 source; region C covers no NO_2 source and is not affected by other sources. Compared to region B, there is a large temporal variety of NO_2 VCDs in region A between three flight lines. Region C is temporally consistent with relatively low NO_2

columns. From these observations it may be concluded that largest temporal variability could occur where there is no local NO_2 source but is down-wind of other sources, especially when wind direction is changing.

7. Line 108: The mobile DOAS measurements are not shown in Figure 5 as stated. However, are shown in Figure 11. Consider adding the location of these measurements in Figure 2 to show where the mobile DOAS measurements were taken. Additionally, in Lines 288-290: technical details about mobile DOAS measurements are not mentioned before this. Discuss these points within Sect 6.2.

We added the location of mobile DOAS measurements in Figure 2, and added technical details about mobile DOAS VCD retrieval method and its uncertainty analysis in Sect 6.2 as stated before.

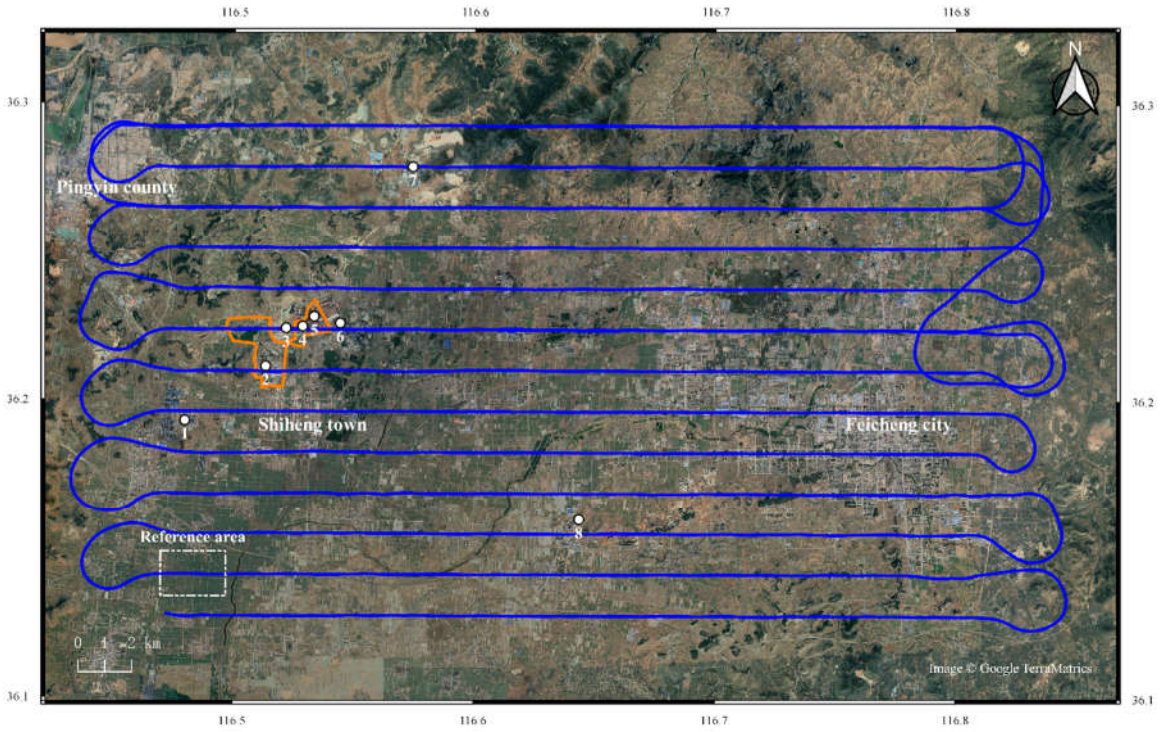

Figure 4. Overview of the Feicheng demonstration flight on 23 June, 2018. Flight lines are shown in blue. Two orange circles represent the routes of mobile DOAS system. White dots numbered from 1 to 8 represent the major emission sources. Number 1: several carbon factories; number 2: a power plant; number 3-6: individual emitters inside the steel factories, while number 4 and 5 are inside the circle of one mobile DOAS route; number 7-8: two cement factories. White dashed box represents the reference area.

8. Line 28: What is the intended meaning behind 'that NOx attracts large attention'. Please elaborate with some details and examples.

Due to rapid industrialization and urbanization in the past few decades, China has become one of the largest NO_x emitters in the world. As a result, China is experiencing a series of severe air pollution problems. Therefore, measuring NO_x distribution by application of different techniques would benefit the pollutant emission detection and the air quality forecast. We modified this paragraph as below:

Nitrogen oxides (NO_x), the sum of nitrogen monoxide (NO) and nitrogen dioxide (NO_2), plays a key role in the chemistry of the atmosphere, such as the ozone destruction in the stratosphere (Solomon, 1999), and the secondary aerosol formation in the troposphere (Seinfeld and Pandis, 2016). In the troposphere, despite lightning, soil emissions and other natural processes, the main sources of NOx are anthropogenic activities like fossil fuel combustion by power plants, factories, and road transportation, especially in the urban and polluted regions. As an indicator of anthropogenic pollution which leads to negative effects both on the environment and human health, the amounts and spatial distributions of NO_x attract large attention. For example, China becomes one of the largest NO_x emitters in the world due to fast industrialization, meanwhile China is also experiencing a series of severe air pollution problems in recent years (Crippa et al., 2018; An et al., 2019). Therefore measuring NOx distribution by application of different techniques, would benefit the pollutant emission detection and the air quality trend forecast (Liu et al., 2017; Zhang et al., 2019).

9. Line 54: add 'of NO2' after spatial distribution to clarify that this is the gas of interest in this paper.

Corrected.

10. Lines 67-68. Figure 1 only shows the optical bench for one of the channels and not all three as implied by the text. Please fix to the text saying that Figure 1 shows the optical bench for channel 3 and that the other two are similar.

Corrected.

Figure 1 shows the optical bench of channel 3 and that the other two are similar. The optical design of each channel comprises a telecentric fore-optics, an Offner imaging spectrometer, and a two dimensional charge-coupled device (CCD) array detector.

11. Line 86-87: reword this sentence to say that spectral and radiometric calibration in the laboratory were done prior to flights to reduce errors in spectral analysis. There shouldn't be a need to state it as 'very necessary'.

Corrected.

12. Line 38: Is this the first space-borne sensor ever in China or the first space-borne sensor related to air quality or trace gases?

The EMI is the first space-borne sensor related to trace gas monitoring, we corrected this in the manuscript.

13. Line 126: clouds were mentioned as filtered out. However, in the rest of the paper it says that the conditions were cloud free. Were there clouds to be filtered? If so, state where and how cloudy it was. If not, state that cloud filtering was not needed for these measurements due to clear skies. Same comment with the sun glint on water if applicable.

The weather condition is cloud free on 23 June, 2018. However, sun glint on water occurred several times in the southern part of flight area (especially over the river near the reference area) because of the low solar zenith angles. We add this statement in the manuscript.

The preprocessing procedure before spectral analysis includes data selection, dark current correction, spatial binning, and in-flight calibration. First, the spectral data acquired during U-turns of aircraft are removed in the processing because of the large and changing orientation angles. Also a threshold of radiance values is set to neglect some over-illuminated ground pixels inside the flight area, which are usually caused by presence of cloud or water mirror reflection. During the entire flight, sun glint on water occurred several times in the southern part of flight area, especially above the river near the reference area. However, cloud was not present due to clean clear-sky weather condition.

14. Line 165: Please revise to say something like 'and the properties that influence radiative transfer of light through the atmosphere' instead of 'and the radiative transfer'

Corrected.

15. Line 184: Please clarify which MODIS AOD product was used.

MODIS AOD product used in this paper is MYD04 on 23 June, 2018, with resampling for every ground UVHIS pixel. We added this in the manuscript.

(5) Aerosol optical Depth (AOD) information used in AMF calculation is MODIS AOD product MYD04 at 470 nm on the same day with resampling for every ground UVHIS pixel (Remer et al., 2005), because neither ground-based aerosol measurement is performed, nor any AERONET station data near the flight area is are available.

16. Line 184: What was the AOD measured from MODIS was during the flight? Please add this detail into the manuscript.

MODIS AOD product used in this paper is MYD04 on 23 June, 2018, with resampling for every ground UVHIS pixel. We added this in the manuscript as stated before.

17. Line 187: Please justify why SSA of 0.93 and asymmetry factor of 0.68 are used.

The SSA and asymmetry factor of aerosol used in the manuscript are estimation of typical urban/industrial aerosols based on previous studies (Li et al., 2018).

Like the NO_2 profile, the aerosol extinction box profile is constructed from the PBL height and AOD. Single scattering albedo (SSA) is assumed to be 0.93, and asymmetry factor is assumed to be 0.68 for aerosol extinction profile, based on previous studies of typical urban/industrial aerosols (Li et al., 2018).

18. Line 226: Is [28] a referring to a reference? Please fix.

Corrected.

19. Consider consolidating Figures 6, 8, and 9 into one figure.

We added an AMF dependency analysis on the VZAs, also a new panel in Figure 8. As shown in Fig. 8 (b) and (c), the changes of AMF are 10% and 7% respectively, when other parameters are set as mean.

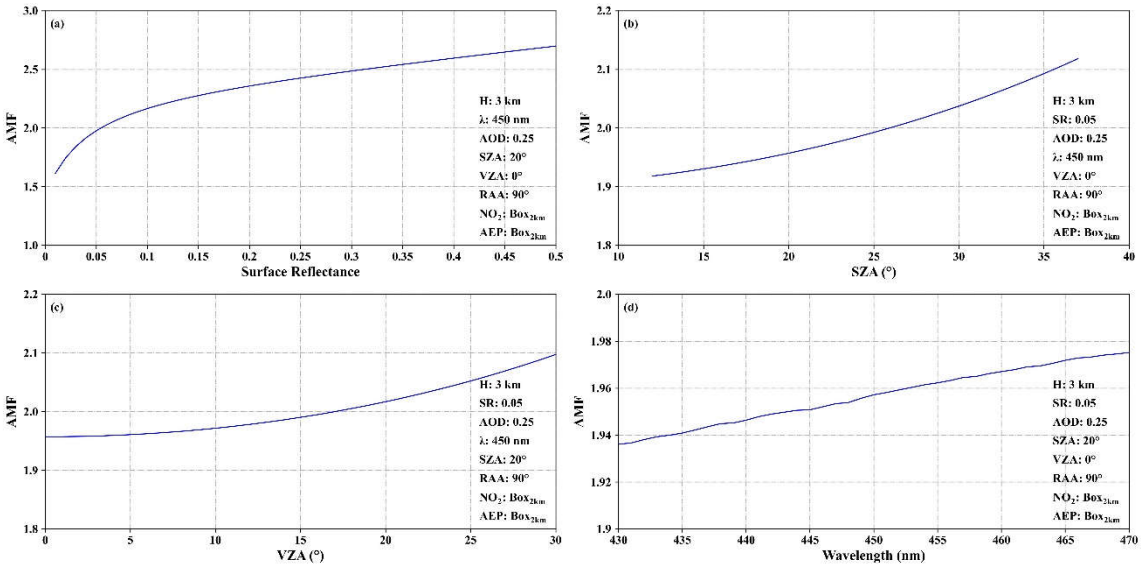

Figure 8. AMF dependence analysis results (a): on the surface reflectance; (b): on the SZAs; (c): on the VZAs; (d): on the wavelength.

20. Line 258: The difference in adjacent flight lines are not 'biases' but rather 'artifacts' of the changing NO2 VCDs due to temporal variation.

Corrected.

21. Section 6 would benefit from a more descriptive title, like 'NO2 VCD Assessment' rather than 'Discussion'

We changed the title of Sect 6 to 'NO_2 VCD Assessment'.

22. Lines 324-325. How do these results change if only considering points with a stricter temporal window between the mobile and aircraft measurements?

We added a new comparison to co-located mobile DOAS measurements only circled the steel factory, and the correlation coefficient improves to 0.86. In this case, all mobile measurements occurred inside the swath of one flight line of aircraft, and the time offset between instruments shortened to 15 minutes.

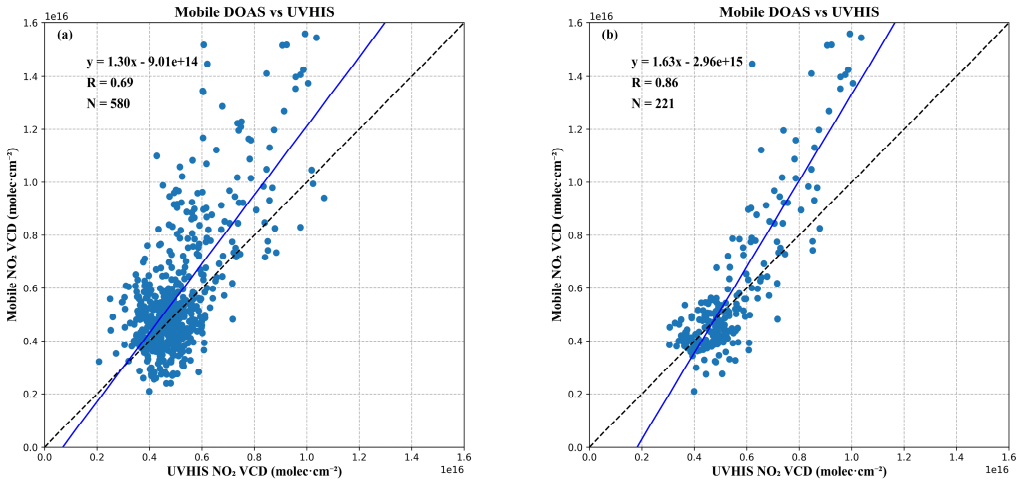

Figure 14. Scatter plot and linear regression analysis of the co-located NO_2 VCDs, retrieved from UVHIS and mobile DOAS system, (a) for all co-located measurements, (b) for co-located measurements that only circled the steel factory.

Figure 14 (a) shows scatter plots with VCDs retrieved by UVHIS on the x-axis and mobile DOAS VCDs on the y-axis, for all co-located measurements. The corresponding results of linear regression analysis are also provided in Fig.14 (a), with a correlation coefficient of 0.69, a slope of 1.30, and an intercept of-9.01 × 10^{14}. The absolute time offset between mobile DOAS and airborne observations can be up to 1 hour, which means that both instruments cannot sample the NO_2 column at certain geolocation simultaneously. As shown in Fig. 14 (b), when only comparing UVHIS VCDs to mobile measurements that circled the steel factory, the correlation coefficient improves to 0.86. In this case, all mobile measurements occurred inside the swath of one flight line of aircraft, and the time offset between instruments shortened to 15 minutes. In general, an underestimation of UVHIS VCDs of increased value can be observed in Fig 14 (a) and (b). Considering the variability in local emissions and meteorology, it is reasonable that the differences between these two instruments exist. Besides, the averaging effect of the area inside an UVHIS pixel can also lead to the underestimation of UVHIS compared to mobile DOAS system.

23. In line 323, the difference between the mobile DOAS measurements and the airborne measurements is described as an 'overestimate' of mobile DOAS measurements, but in the conclusions and abstract it is stated as an 'underestimate' by the aircraft. Please be consistent in this description in the manuscript.

Corrected.

24. Figure 2: the black dots are hard to see. Please change the color and/or symbol to make the points of interest stand out.

We updated Figure 2 as stated before.

25. Instead of having Table 2, could those results be translated into Figure 3(a) somehow? If keeping Table 2, then be more descriptive in the caption to say these are FWHMs at these wavelengths/angles.

We added more information in the title of Table 2, also we added a new figure to plot the slit function shapes of 9 viewing angles at 450.504 nm.

Table 2. Preflight wavelength calibration results (FWHMs) of UVHIS channel 3 for 9 viewing angles. Light sources used in the calibration are a mercury-argon lamp and a tunable laser. Slit function shapes are retrieved by least square fitting of characteristic spectral lines, using a symmetric Gaussian function.

FOV	379.887 nm	404.656 nm	450.504 nm	500.566 nm
-20°	0.35 nm	0.35 nm	0.39 nm	0.50 nm
-15°	0.33 nm	0.31 nm	0.33 nm	0.43 nm
-10°	0.31 nm	0.29 nm	0.29 nm	0.41 nm
-5°	0.31 nm	0.30 nm	0.29 nm	0.34 nm
0°	0.31 nm	0.32 nm	0.30 nm	0.30 nm
5°	0.34 nm	0.36 nm	0.34 nm	0.30 nm
10°	0.38 nm	0.39 nm	0.38 nm	0.32 nm
15°	0.40 nm	0.44 nm	0.42 nm	0.35 nm
20°	0.45 nm	0.46 nm	0.47 nm	0.38 nm

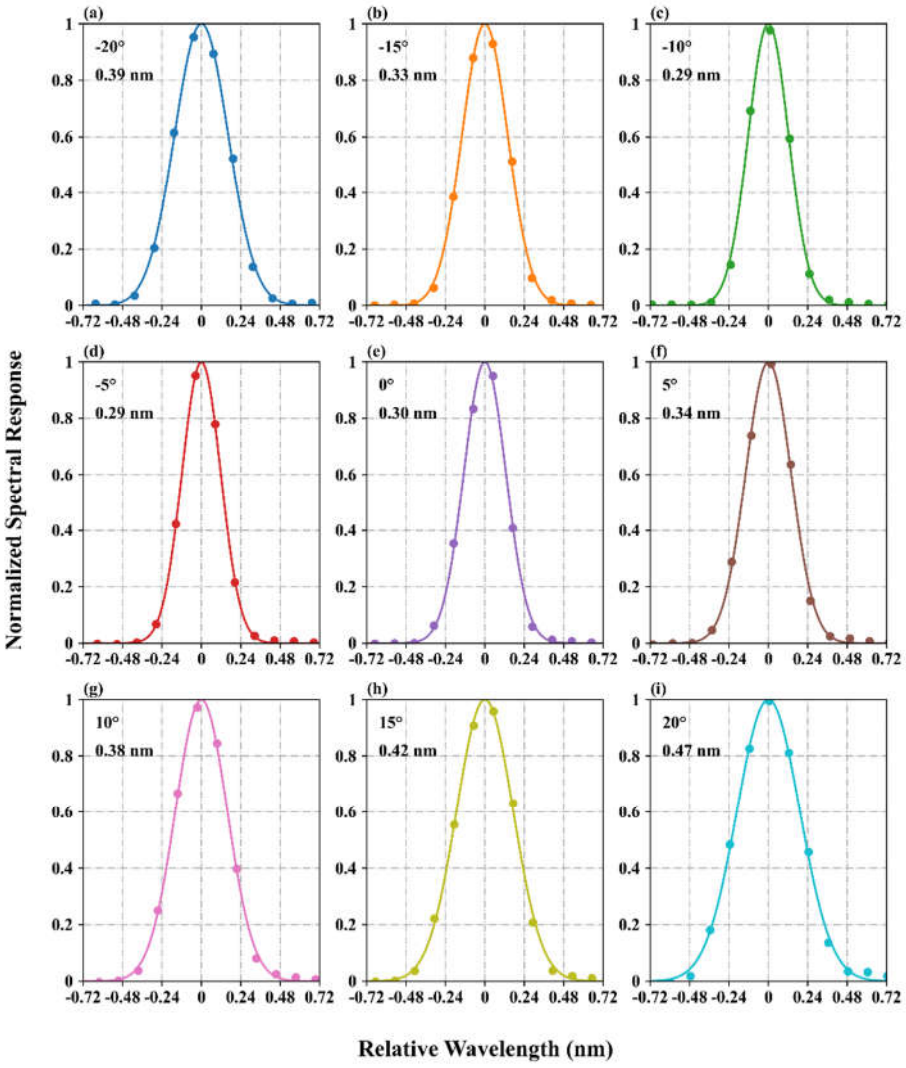

Figure 2. Measured slit functions (dots) at 450.504 nm and retrieved slit function shapes (lines) using a symmetric Gaussian function for 9 viewing angles.

275

26. Lines 110-113: This text is redundant. These details were already stated in the previous paragraph.

We reorganize this paragraph as below:

In the condition of spatial binning by 10 pixels across-track, the across-track spatial resolution of the ground pixel is about 22 m. At typical aircraft ground speed of 50 m/s and integration time of 0.5 s, the along-track spatial resolution of the ground pixel is about 25 m.

27. Similarly, the first two paragraphs in Section 5 appear to be redundant. Please consolidate into one paragraph without repeating details already stated.

We reorganize Sect 5 as below:

The NO_2 tropospheric VCD two-dimensional distribution map is shown in Fig. 10 for the research flight on 23 June 2018. With a high performance of UVHIS in spectral and spatial resolution, Figure 10 shows fine-scale NO_2 spatial variability to resolve individual emission sources. In general, the NO_2 distribution is dominated by several exhaust plumes with enhanced NO_2 concentration in the northwest part, which share a transportation pattern from south to north consistent with the wind direction. These sources include a power plant, a steel factory, two cement factories, and several carbon factories. The largest plume with peak values of up to 3×10^{16} molec cm^{-2}, originates from an emitter inside a steel factory (number 3 in Fig. 10). This dominant plume reaches its peak value outside at a small valley about 1 km north of the factory, and is transporting at least 9 km and seems to be continuing outside the flight region. This enhanced level of NO_2 may be caused by terrain factor which contributes to the accumulation of pollution gases.

Number 4 to 6 represent other emitters inside the steel factory. While the exhaust plumes originated from number 4 and 5 merge with the dominant plume, the plume from number 6 transports to north individually with a peak value of 1.4×10^{16} molec cm^{-2}. A weaker plume with peak values of 1.5×10^{16} molec cm^{-2} is also detected by UVHIS, which seems to originate from the power plant. Indicated by number 2 in Fig. 10, this power plant is less than 2 km south of the steel factory. Number 1 in Fig. 10 indicates several carbon factories, which are located on the left side of the flight area. Several plumes with peak values of 1.5×10^{16} molec cm^{-2}, gradually merge together during transportation downwind. Number 7 and Number 8 in Fig. 10 represent two different cement factories. Peak values of these two plumes are 1.5×10^{16} molec cm^{-2} and 1.4×10^{16} molec cm^{-2} respectively.

Compared to the industrial areas mentioned above, the pollution levels of the rural areas are much lower due to the lack of contributing sources, ranging from 2 to 6×10^{15} molec cm^{-2}. The urban area of Feicheng city is located on the right side of the flight area. Figure 11 is an enlarged map of UVHIS NO_2 observations over Feicheng city, with a color scale only extends to 7×10^{15} molec cm^{-2}. Two black lines in Fig. 11 represent the truck roads in this city. The S104 is a provincial highway that crosses Feicheng from north to south, while the S330 crosses Feicheng from east to west. Although lots of noise can be observed in Fig. 11, the NO_2 sources in Feicheng are mainly related to traffic and concentrated along the S104.

Due to temporal discontinuity of flight lines and dynamic characteristics of NO_2 field, artefacts can be observed between adjacent flight lines. Figure 12 shows three flight lines that pass through the steel factory, at local time 13:26 (a), 13:32 (c), and 14:57 (b). Panel (a) and (b) represent flight lines that cover the same area with a 1.5 hour time gap, panel (a) and (c) represent adjacent flight lines with a 6 minutes time gap. These flight lines can be divided into three regions: region A covers no NO_2 source but is affected by carbon factories about 3 km away; region B covers the steel factory as dominant NO_2 source; region C covers no NO_2 source and is not affected by other sources. Compared to region B, there is a large temporal variety of NO_2 VCDs in region A between three flight lines. Region C is temporally consistent with relatively low NO_2 columns. From these observations it may be concluded that largest temporal variability could occur where there is no local NO_2 sources but is down-wind of other sources, especially when wind direction is changing.

28. There are grammar mistakes throughout the manuscript. These errors will need to be fixed before publication but I expect will be evolving in revisions. Some grammar and other writing fixes are located at the bottom of this review to help gives examples as to the types of errors found. They are not a full edit.

Corrected.

29. Consider a more concise title, such as, 'The first high-resolution NO2 observations from the Ultraviolet Visible Hyperspectral Imaging Spectrometer (UVHIS)'.

We changed the title of the manuscript to 'The first high-resolution tropospheric NO_2 observations from the Ultraviolet Visible Hyperspectral Imaing Spectrometer (UVHIS)'.

30. Does EMI capture this area? Or TROPOMI? It would be interesting to show some comparisons to those data products, especially since the flight was early afternoon on a cloud free day.

Both EMI and TROPOMI capture this area on 23 June, 2018. In the figure below, we plot TROPOMI tropospheric NO_2 vertical columns because of its high spatial resolution. A quantitative comparison of the two retrievals may not make much sense because we use TROPOMI product to estimate the reference residual. However, enhancements in TROPOMI NO_2 are consistent with large UVHIS columns inside the flight area. Also, enhancements in TROPOMI NO_2 columns to the north of the flight area may indicate that the plumes originated from the steel factory keep transporting for tens of kilometers.

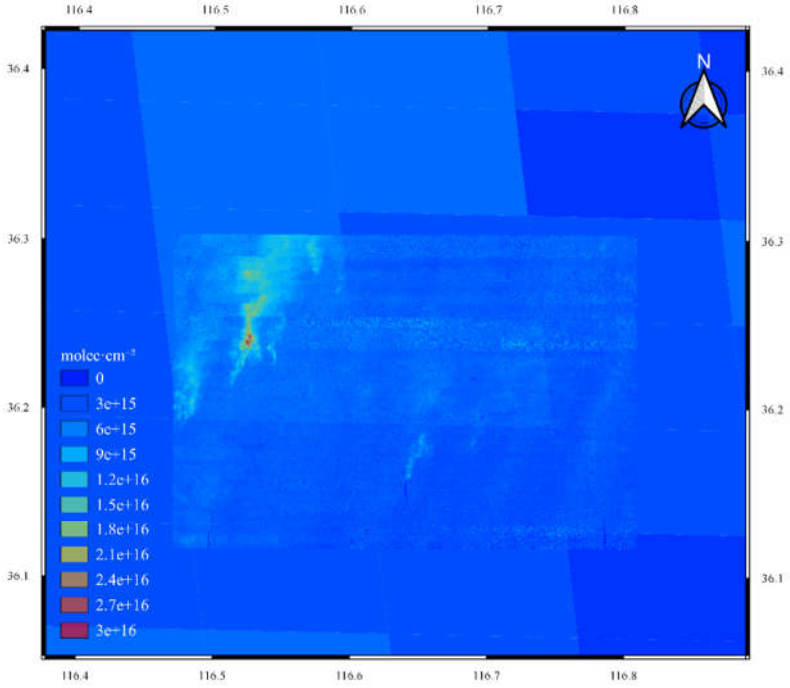

345 *31. What does Feicheng City look like if mapped on a color scale that only extends to 5x1015. Are there spatial patterns captured? It is hard to see any patterns in Figure 10 in that area due to the color scale expanding to much larger pollution scales. Perhaps a second panel in this figure would be interesting.*

We added a new figure of enlargement of UVHIS NO_2 VCD map over Feicheng city as below. More details can be found in answer to question No. 27.

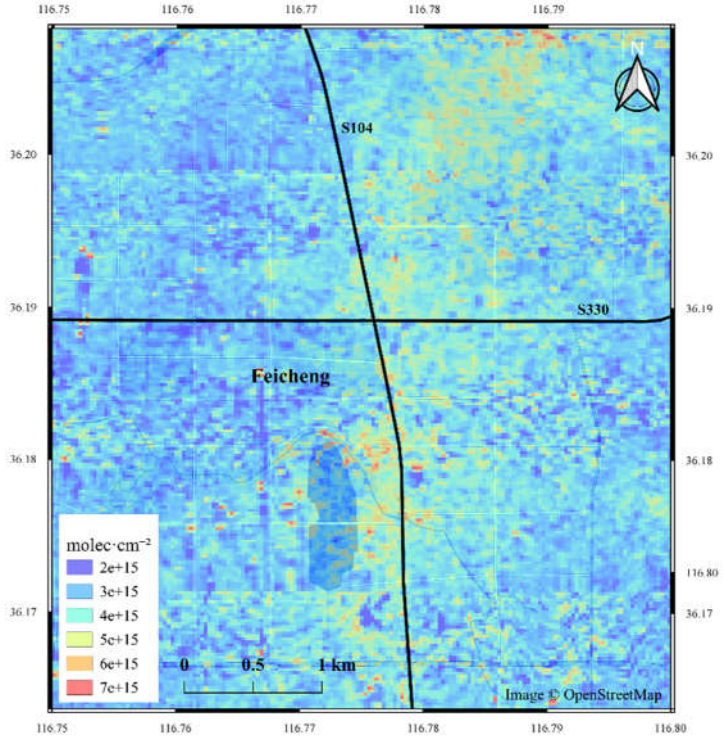

Figure 11. Enlargement of UVHIS NO_2 VCD map over Feicheng city with a color scale only extends to 7×10^{15} molec cm^{-2}. Two black lines in the map represent two truck roads that cross Feicheng city: S104, and S330.

32. Figure 7: consider adding a true color image of this line to compare with the surface reflectance and AMF.

For better comparison with surface reflectance and AMF, we added a panel in Figure 9 of radiance measurements from UVHIS. It is obvious that all panels share a same spatial distribution. However, some small differences can be observed due to time offset and spatial resolution difference.

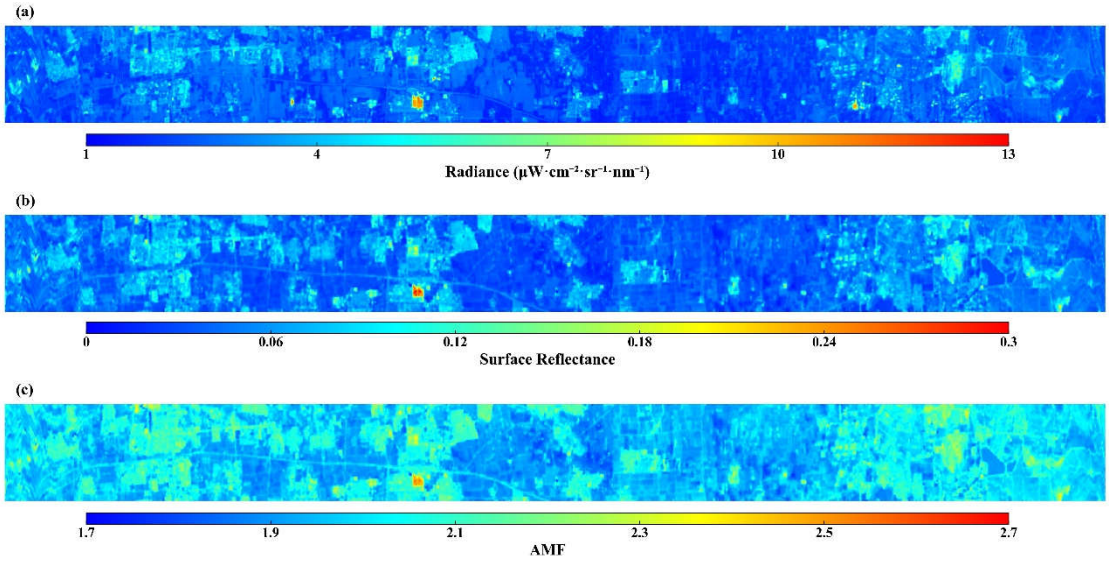

Figure 9. (a) UVHIS Measured radiance; **(b)** Landsat 8 Surface reflectance; (c) computed AMFs, for one flight line of the Feicheng data set. A strong dependency of the AMF on the surface reflectance can be observed.

33. Can you comment on applications of the other channels for UVHIS? Are there plans for other products in the future?

The UVHIS is part of a full spectral multimodal airborne imaging spectrometer. Our works only involve the channel 2 and 3 for trace gas measurements. In future works, we will present the retrieval results of SO_2 or HCHO based on measurements of channel 2. For channel 1 that covers deep UV spectral range, it is beyond our scope of work, and it may be used for wildfire or other artificial UV light source detection.

Authors' Response to Comments from anonymous referee #2

Black, italic: Referee's comments

Blue: Author's reply

Red: Changes in the original discussion paper

Xi et al. present a new airborne imaging DOAS instrument and results of the first demonstration flight. The results are encouraging and data might be interesting for further analysis such as satellite validation, emission estimates or model comparison. The paper fits very well in the context of AMT. However at some points more details might be required by the reader. Most of them are not critical but require an update of the manuscript.

First, we appreciate the overall positive response of the referee and we would like to thank for his constructive comments and helpful suggestions on the manuscript. As described below, we have modified the manuscript according to suggestions and provided clarifications where necessary.

1. Through out the manuscript the authors should take care to distinguish between total and tropospheric vertical columns - in most cases the tropospheric vertical column or to be more precise the column below the flight altitude is meant e.g. l 167.

In this manuscript, the NO_2 vertical columns we calculated are tropospheric vertical columns. We added necessary clarification throughout the manuscript. For example, we changed the title of the manuscript to 'The first high-resolution tropospheric NO2 observations from the Ultraviolet Visible Hyperspectral Imaing Spectrometer (UVHIS)'.

2. The NO2 fit shown in figure 4 has some residual structures, which might be noise but might also be caused by a systematic issue. The instrument was carefully calibrated before the measurements. The wavelength calibration is used only as apriori for the QDOAS software - which is certainly necessary. The slit function shape that can be extracted from the measurements using the Mercury-Argon lamp but are not shown or mentioned. Instead a symmetric Gaussian slit function is assumed in the DOAS analysis. The width of the slit function varies significantly within the fitting window (figure 3) - maybe the shape does so as well? I suggest adding at least a figure of the measured slit function for the extreme viewing directions (left, centre and right) including the Gaussian fit.

We added a figure of measured slit functions at 450.504 nm for 9 viewing angles (-20°, -15°, -10°, -5°, 0°, 5°, 10°, 15°, 20°), and the respective Gaussian fit results. These Gaussian fit results suggest that a symmetric Gaussian function is a reasonable assumption for slit shape in all viewing directions.

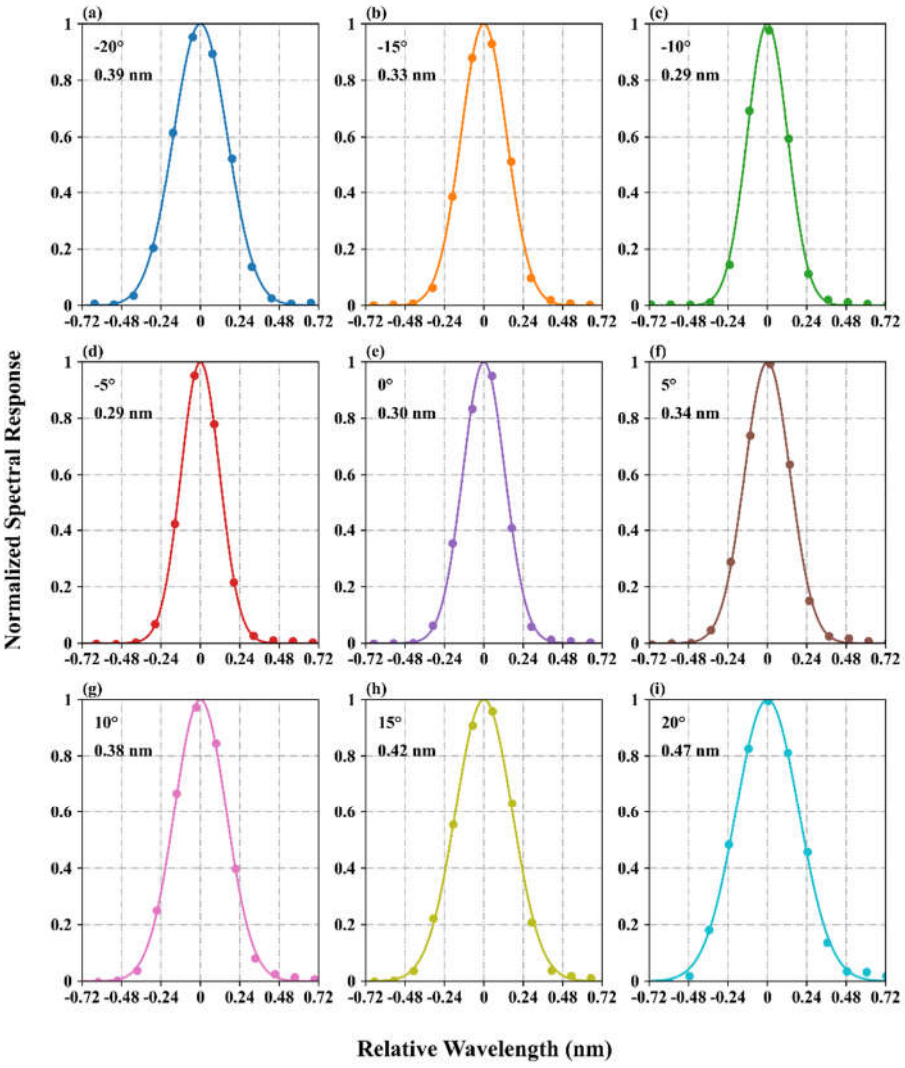

Figure 2. Measured slit functions (dots) at 450.504 nm and retrieved slit function shapes (lines) using a symmetric Gaussian function for 9 viewing angles.

The preflight wavelength calibration was also performed in the laboratory, using a mercury–argon lamp and a tunable laser as light sources. We model the slit function of UVHIS using a symmetric Gaussian function. Spectral registration and slit function calibration are achieved by least square fitting of characteristic lines in collected spectra. Table 2 lists the retrieved full-width at half maximums (FWHMs) for channel 3. Figure 2 shows the measured slit functions at 450.504 nm for 9

viewing angles (-20°, -15°, -10°, -5°, 0°, 5°, 10°, 15°, 20°), and respective retrieved slit function shapes using a symmetric Gaussian function. These Gaussian fit results suggest that a symmetric Gaussian function is a reasonable assumption for slit shape in all viewing directions.

3. The observations partly overlap as the distance between the parallel flightracks was 1.5 km and the swath width is 2.2 km. How good do the observed tropospheric NO2 columns agree in the overlapping regions, does this depend on the flight direction and time, according to figure 2 some parts of the flight track were covered at least twice.

Indeed, several fight lines are repeated in the northern part of flight area, but the spectral data of UVHIS are not recorded because of misoperation. Only spectral data of the flight lines over the steel factory are recorded, and the pass time of aircraft is 13:26 and 14:57 respectively. We added a paragraph and a figure to discuss this in detail.

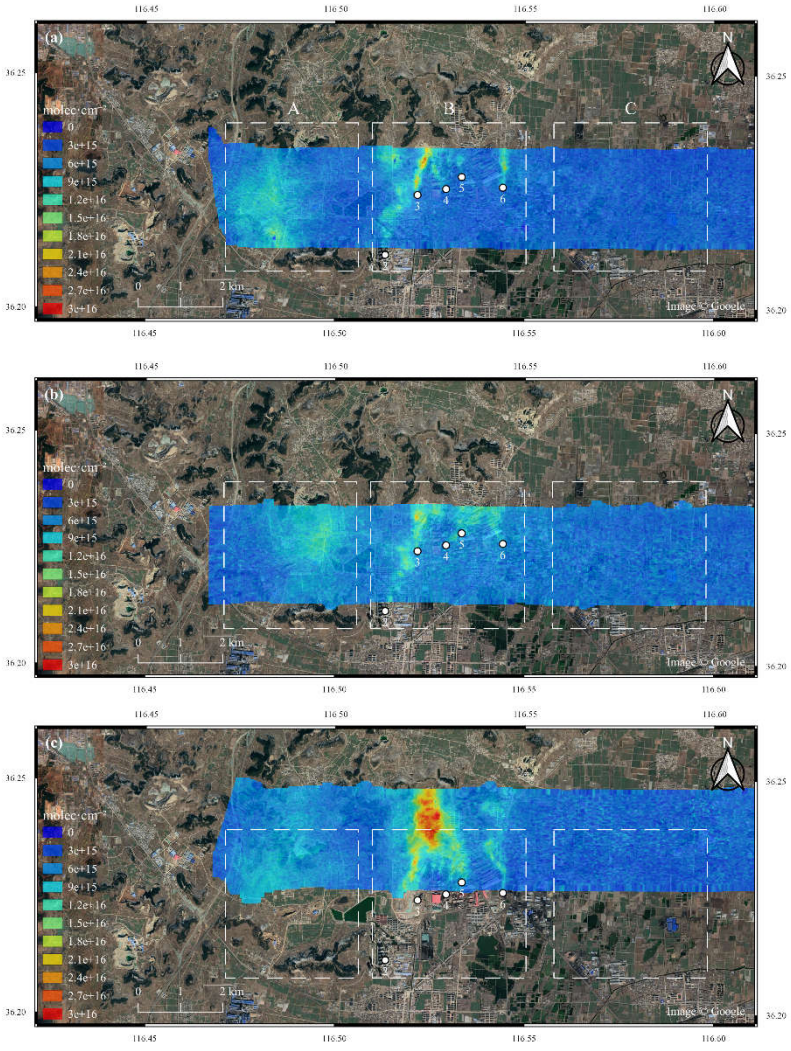

Figure 12. Three flight lines that pass through the steel factory, at local time 13:26 (a), 13:32 (c), and 14:57 (b). Panel (a) and (b) represent flight lines that cover the same area with a 1.5 hour time gap, panel (a) and (c) represent adjacent flight lines with a 6 minutes time gap.

Due to temporal discontinuity of flight lines and dynamic characteristics of NO_2 field, artefacts can be observed between adjacent flight lines. Figure 12 shows three flight lines that pass through the steel factory, at local time 13:26 (a), 13:32 (c), and 14:57 (b). Panel (a) and (b) represent flight lines that cover the same area with a 1.5 hour time gap, panel (a) and (c) represent adjacent flight lines with a 6 minutes time gap. These flight lines can be divided into three regions: region A covers no NO_2 source but is affected by carbon factories about 3 km away; region B covers the steel factory as dominant NO_2 source; region C covers no NO_2 source and is not affected by other sources. Compared to region B, there is a large temporal variety of NO_2 VCDs in region A between three flight lines. Region C is temporally consistent with relatively low NO_2

columns. From these observations it may be concluded that largest temporal variability could occur where there is no local NO_2 source but is down-wind of other sources, especially when wind direction is changing.

4. The error given here is not the fitting error but the total error of the VCD - even if the fitting error ~4.8 x 10^15 molec/cm^2 is probably the dominant contribution.

Corrected.

5. The instrument was build for airborne measurements in the troposphere, however the spectral range encompasses the deep UV from 200-276 nm in channel 1, I am afraid the intensity in this channel will be very low. Through out the manuscript the data from the channels 1 and 2 are not shown nor used. Airborne measurements often face the problem of the instruments being too heavy, therefore I am surprised to read that the instruments has a channel 1 that seems not very useful. Maybe the authors can briefly comment about the potential use of the channels 1 and 2, or the former use in a different instrument. For channel 2 I can think of the retrieval of SO2 or HCHO, both would interesting for the presented study but may require a more detailed analysis.

The UVHIS is part of a full spectral multimodal airborne imaging spectrometer. Our works only involve the channel 2 and 3 for trace gas measurements. In future works, we will present the retrieval results of SO_2 or HCHO based on measurements of channel 2. For channel 1 that covers deep UV spectral range, it is beyond our scope of work, and it may be used for wildfire or other artificial UV light source detection.

6. The figure of the instrument (figure 1) is a bit confusing it might be clearer if the authors reduce the number of light beams. It seems that part of the "red" light beam originating from the "top" is blocked by the convex grating, I suppose this is not the case, maybe because it is shifted relative to the drawing plane in the third dimension? Does second perspective view helps to explain more clearly? A radiometric calibration was performed as well as a spectral calibration. However, it seems the data form the radiometric calibration were not used it might be interesting to see the calibrated intensity in comparison to the LANDSAT 8 albedo (figure 7).

We replot Figure 1 with less number of light beams in the manuscript, also another figure added here would help to explain the structure more clearly.

For better comparison with surface reflectance and AMF, we added a panel in Figure 9 of radiance measurements from UVHIS. It is obvious that all panels share a same spatial distribution. However, some small differences can be observed due to time offset and spatial resolution difference.

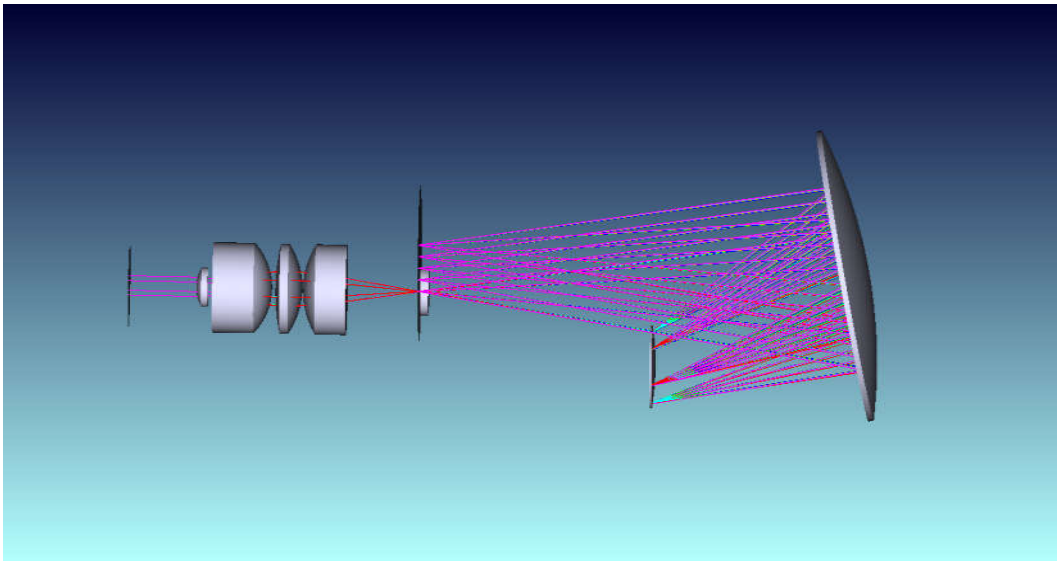

475

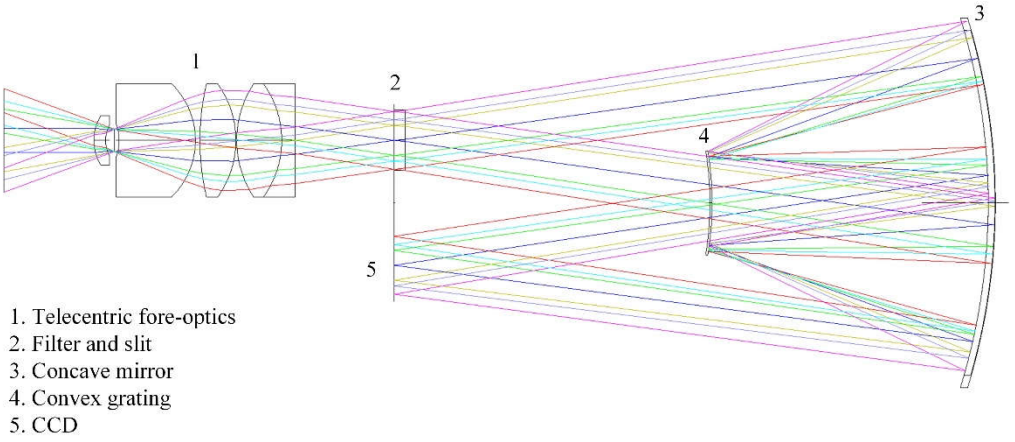

Figure 1. Optical layout of the UVHIS channel 3. Optical design of channel 1 and channel 2 is similar.

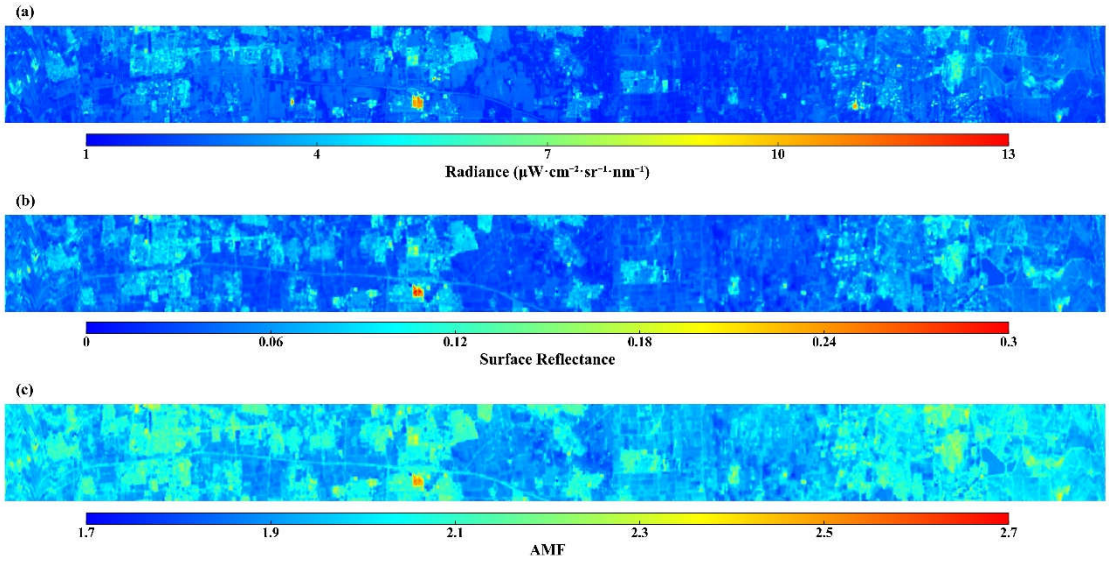

Figure 9. (a) UVHIS Measured radiance; (b) Landsat 8 Surface reflectance, (c) computed AMFs, for one flight line of the Feicheng data set. A strong dependency of the AMF on the surface reflectance can be observed.

7. Parts of CCD are blocked to control offset and dark current which is a good idea if this part of the CCD can not be used for real observation. However in section 4 the well established pre-flight dark current and offset measurements are used and the dark measurements at the edges of the CCD are not mentioned.

Both pixels at left and right edge on the CCD detector are blocked to monitor dark current. During the flight, signals from these pixels are very stable due to the temperature stability of the instrument. For dark current correction, we prefer to use pre-flight dark current measurements for the entire CCD detector because the dark measurements at the edges of the CCD only cover a small part of the CCD.

8. For non Chinese readers some more details about the measurement area might be nice to have. Can you add a map of China indicating where the city of Feiching is and in the context of the paper a satellite observation of NO2 for the day or season might be included as well.

Feicheng is a county-level city in Shandong province, China, about 410 km away from Beijing. The flight area is located on the south bank of the Yellow River, at the western foot of Mount Tai. We added a figure of TROPOMI NO_2 tropospheric observation on 23 June, 2018, with the background Google map and the location of Feicheng.

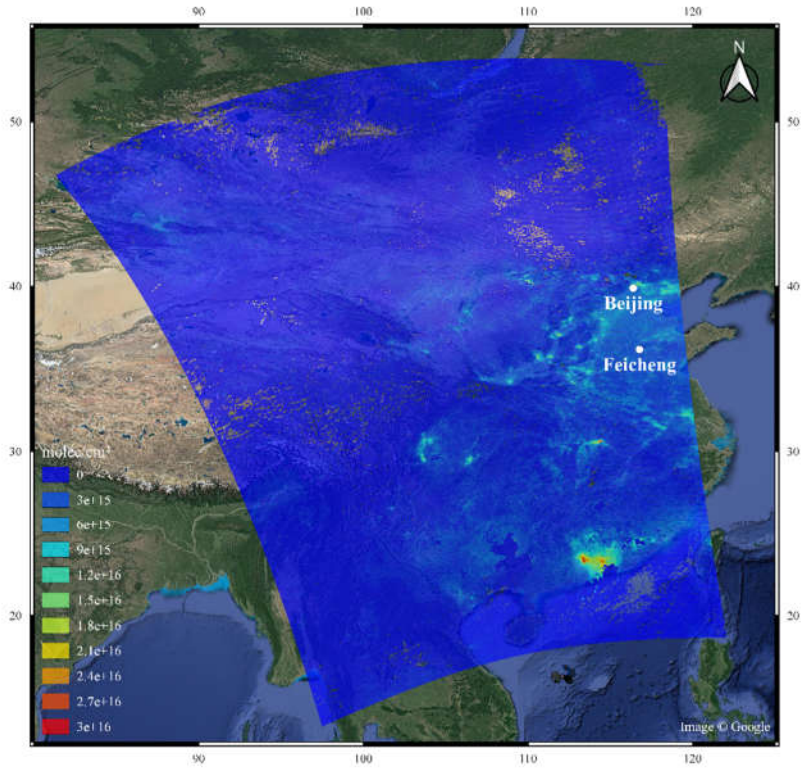

Figure 3. TROPOMI observation of tropospheric NO_2 over China on 23 June, 2018. The location of UVHIS flight (Feicheng city) is also plotted in the map.

9. The authors use a wavelength range between 430 and 470 nm for the DOAS analysis including the cross sections of NO2, O3 and O4, as well as the ring cross section. However water vapour also shows some strong absorption lines in the respective wavelength range (Hitran data base, Rothman 2013), this is not included in the DOAS fit. (see general comment)

We recalculated the NO_2 dSCD by adding a H_2O vapor cross section from HITRAN database. The DOAS fit results and the errors both decreased slightly. For the fit example in the manuscript, the dSCD decreased from $5.05 \pm 0.38 \times 10^{16}$ molec cm^{-2} to $4.95 \pm 0.34 \times 10^{16}$ molec cm^{-2}, while the RMS decreased from 4.56×10^{-3} to 4.27×10^{-3}. We also updated the DOAS fit example figure.

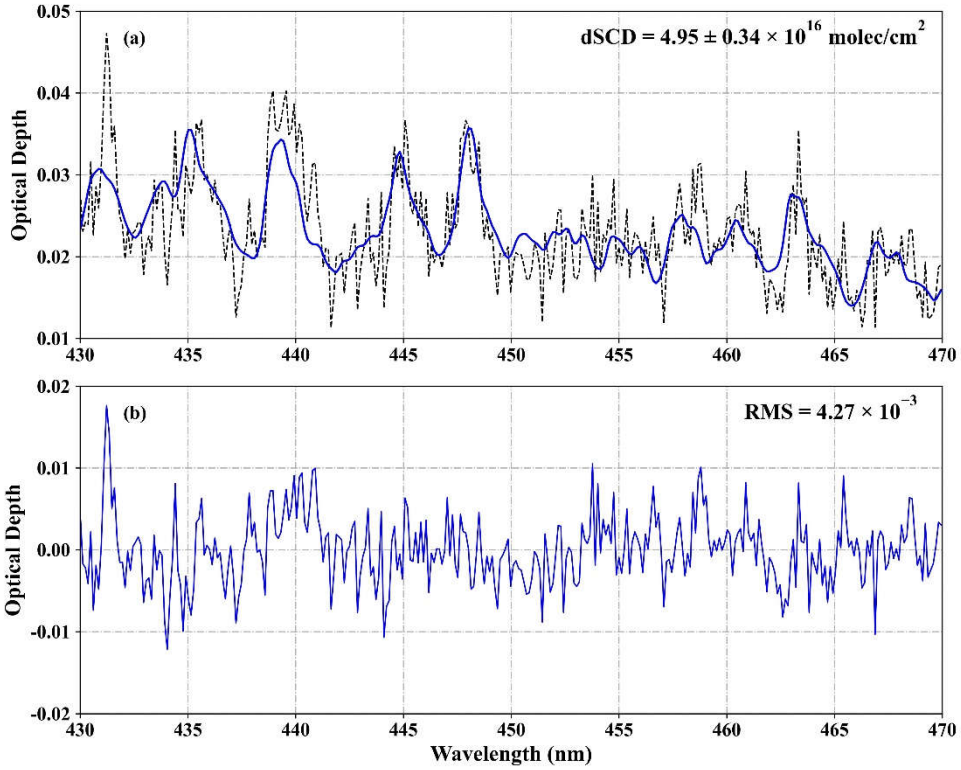

Figure 6. Sample DOAS fit result for NO_2: (**a**) observed (black dashed line) and fitted (blue line) optical depths from measured spectra; (**b**) the remaining residuals of DOAS fit.

10. The tropospheric background of 1 x 10^15 molec/cm^2 as given by Popp et al. (2012) refers to the background around Zürich I am not sure this can be assumed for China as well. Here a satellite observation of the rural background around Feiching might help to estimate a realistic background.

We agree that a satellite observation of the rural area around Feicheng would be a more realistic background estimation. We modified the tropospheric NO_2 vertical column of reference spectra to 3×10^{15} molec cm^{-2} with error of 1×10^{15} molec cm^{-2} based on TROPOMI NO_2 product on the same day. We also updated the UVHIS NO_2 distribution map.

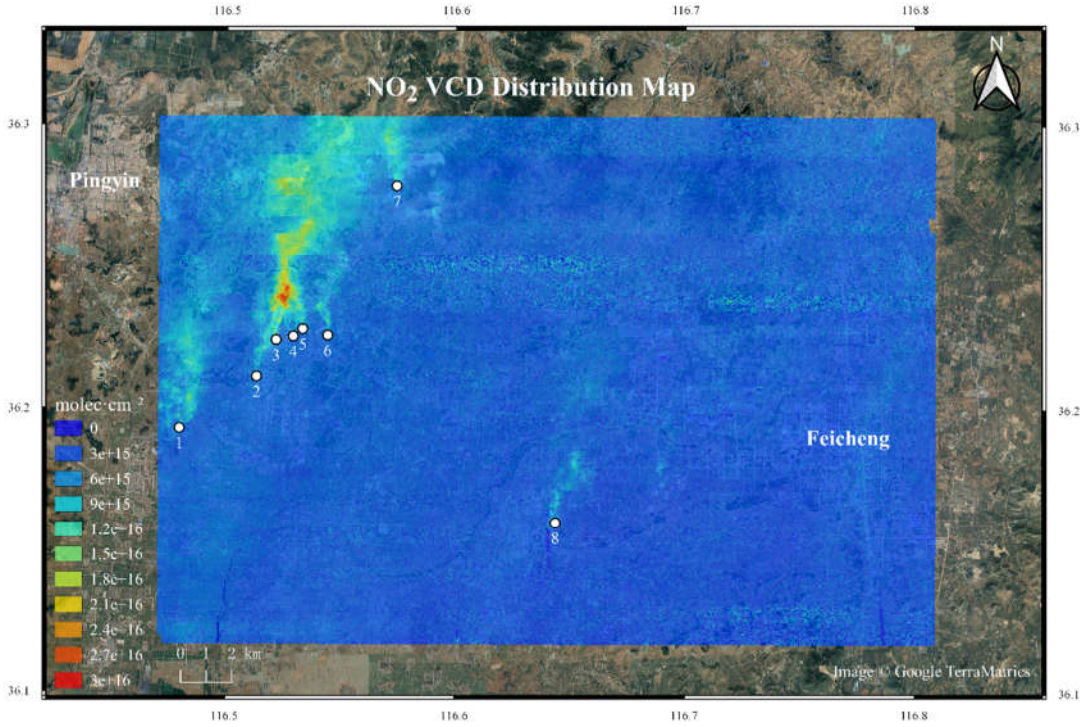

Figure 10. Tropospheric NO_2 VCD map retrieved from UVHIS over Feicheng on 23 June 2018. The major contributing NO_2 emission sources are indicated by number 1 to 8.

11. The section about the Landsat 8 data analysis and resolution might be shifted from section 4.3.2 to 4.3.1. Meier et al. 2017 developed a method to retrieve the albedo from the measurements did you consider applying a similar method?

We shifted the section about the Landsat 8 data analysis and resolution from section 4.3.2 to 4.3.1. We realize that Meier et al. (2017) developed a method to retrieve surface reflectance from an instrument which is not radiometrically calibrated. However, surface reflectance algorithm for UVHIS is still under development and needs to be verified. We will include this in future works.

12. The assumption about the aerosol optical density, SSA and scattering function are partly given but not justified, the details about the optical density are not given directly.

MODIS AOD product used in this paper is MYD04 on 23 June, 2018, with resampling for every ground UVHIS pixel. The SSA and asymmetry factor of aerosol used in the manuscript are estimation of typical urban/industrial aerosol based on previous studies (Li et al., 2018).

(5) Aerosol optical Depth (AOD) information used in AMF calculation is MODIS AOD product MYD04 at 470 nm on the same day with resampling for every ground UVHIS pixel (Remer et al., 2005), because neither ground-based aerosol measurement is performed, nor any AERONET station data near the flight area is are available. Like the NO_2 profile, the aerosol extinction box profile is constructed from the PBL height and AOD. Single scattering albedo (SSA) is assumed to be 0.93, and asymmetry factor is assumed to be 0.68 for aerosol extinction profile, based on previous studies of typical urban/industrial aerosols (Li et al., 2018).

13. During ascent and decent of the plane you can often estimate the PBL height from visibility or if available dew point measurements. This might be more realistic than the typical summer day assumption of 2000 m. However, the measurements were performed 2 years ago the respective information might be lost. The error is less than 13%, assuming that the PBL reached at least up to 1000 m.

The PBL height was not measured during the flight on 23 June, 2018. Unfortunately, other respective information about PBL height was not available at present.

14. The measurements by Tack et al. (2017) were performed in an SZA range of 40 to 60 degree; in this range the effect of the SZA might be different as in the range between 10 and 40 degree.

We added an AMF dependency analysis on the VZAs, also a new panel in Figure 8. As shown in Fig. 8 (b) and (c), the changes of AMF are 10% and 7% respectively, when other parameters are set as mean.

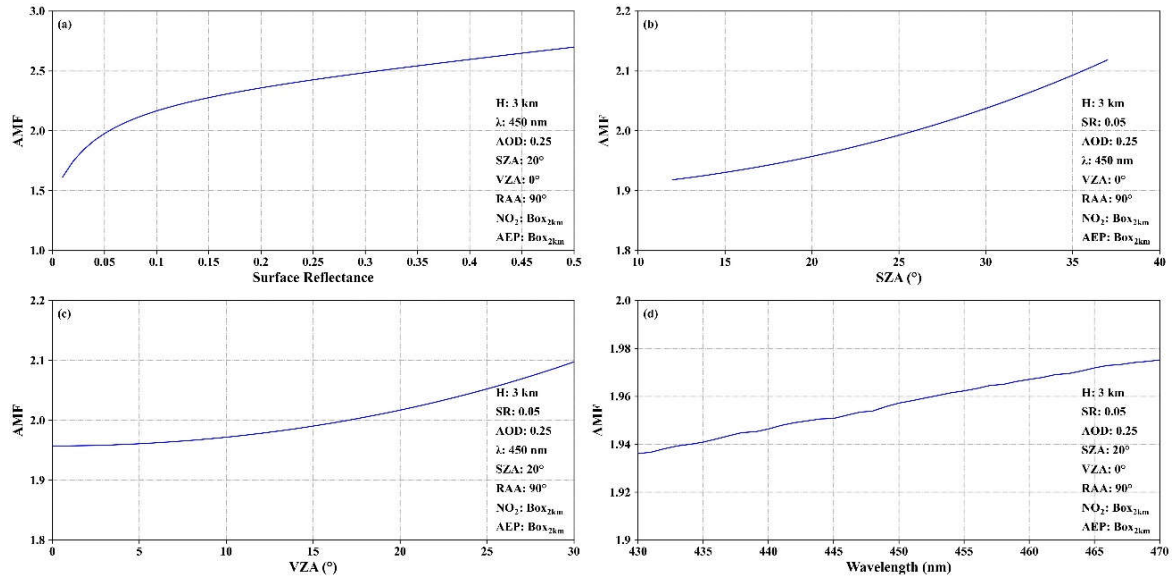

Figure 8. AMF dependence analysis results (a): on the surface reflectance; (b): on the SZAs; (c): on the VZAs; (d): on the wavelength.

As can be seen in Fig. 7, the effect of sun and viewing geometries on AMFs is very small. Based on a previous study from Tack et al. (2017), changing SZA have the greatest effect on AMFs, in comparison to other sun and viewing geometries. In this study, we also did an AMF dependence analysis on SZAs and VZAs. The SZA varies from 12.8° to 37.4° during the 3 hour research flight, while the VZA ranges from 0° to 30° in most cases. As shown in Fig. 8 (b) and (c), the changes of AMF are less than 10% and 7% respectively, when other parameters are set as mean. Generally, a larger SZA or a larger VZA could result a longer light path through the atmosphere and thus a larger AMF.

15. The uncertainty of the cross section is usually dominated by systematic uncertainty and not by the random errors. Only the random part is included in the QDOAS error analysis.

We agree that the uncertainty of the cross section is usually dominated by systematic uncertainty. We added the word 'systematic' in this sentence.

16. For the reference region a vertical column of 1 x10 ˆ15 molec/cmˆ2 is assumed, therefore for the error of the slant column it should be multiplied by the respective AMF.

We modified the tropospheric NO_2 vertical column of reference spectra to 3×10^{15} molec cm^{-2} with error of 1×10^{15} molec cm^{-2} based on TROPOMI NO_2 product. Also, we fix this error in the calculation of error budget. The mean total value of error is 3.0×10^{15} molec cm^{-2} with a range from 1.5 to 5.9×10^{15} molec cm^{-2}.

The second uncertainty source, σ_{SCDref}, is caused by the NO_2 residual amount in the reference spectra. Since we use TROPOMI tropospheric NO_2 product of the clean reference area as background amount, the uncertainty of NO_2 vertical column is estimated to be 1×10^{15} molec cm^{-2} directly from TROPOMI product. Assuming a tropospheric AMF of 2.0 and a tropospheric AMF over the reference spectra of 1.8, this results an uncertainty 9×10^{14} molec cm^{-2} to the tropospheric vertical column.

17. The focus of the paper is on the airborne instrument. A proper reference to the mobile DOAS instrument should be given, if this is not possible it might worth adding some additional information. Is the tropospheric or the total NO2 column retrieved? How large are the uncertainties of the mobile instrument? Are the same AMF settings (albedo, PBL height, aerosols) used as for the airborne observation?

We added two paragraphs in Sect 6.2 to describe the mobile DOAS tropospheric NO_2 retrieval method and its uncertainty analysis. For better comparison with UVHIS NO_2 observations, assumptions and parameters in NO_2 retrieval method for the mobile DOAS were set to the same as the UVHIS.

For better comparison with UVHIS NO_2 observations, assumptions and parameters in NO_2 retrieval method for the mobile DOAS were set to the same as the UVHIS. For example, residual amount of NO_2 in reference spectra was set to 3×10^{15} molec cm^{-2} with an error of 1×10^{15} molec cm^{-2}; mobile DOAS observations only focus on tropospheric portion of NO_2 columns, assumed that the difference of the stratospheric NO_2 columns between observed spectra and reference spectra is negligible; vertical profiles of NO_2 and aerosol extinction, albedo, and aerosol properties in the AMF calculation were set to the same as UVHIS.

Like the uncertainty analysis of UVHIS NO_2 columns, the total uncertainty on the retrieved mobile tropospheric VCD is composed of three parts: (1) the mean uncertainty on dSCD of mobile DOAS is 1.4×10^{15} molec cm^{-2}; (2) the uncertainty of reference vertical column is estimated to be 1×10^{15} molec cm^{-2}. In the case that the tropospheric AMFs of measured and reference spectra are very close, this part results an uncertainty 1×1015 molec cm^{-2} to the total uncertainty; (3) the mean relative uncertainty on the AMF calculation is 22 % by square root of the quadratic sum of individual uncertainties like UVHIS. Combining these uncertainties together, the mean total uncertainties on the retrieved tropospheric NO_2 VCDs is 2.1×10^{15} molec cm^{-2}.

18. Please add an approximate scale in figure 2 or write some comparable information in the caption e.g. the measurement area was ~20 x 30 km and the distances between parallel lines were 1.5 km In figure 10 the individual sources are numbered it might help to add the numbers already in figure 2 in addition to the description.

We updated this figure as below:

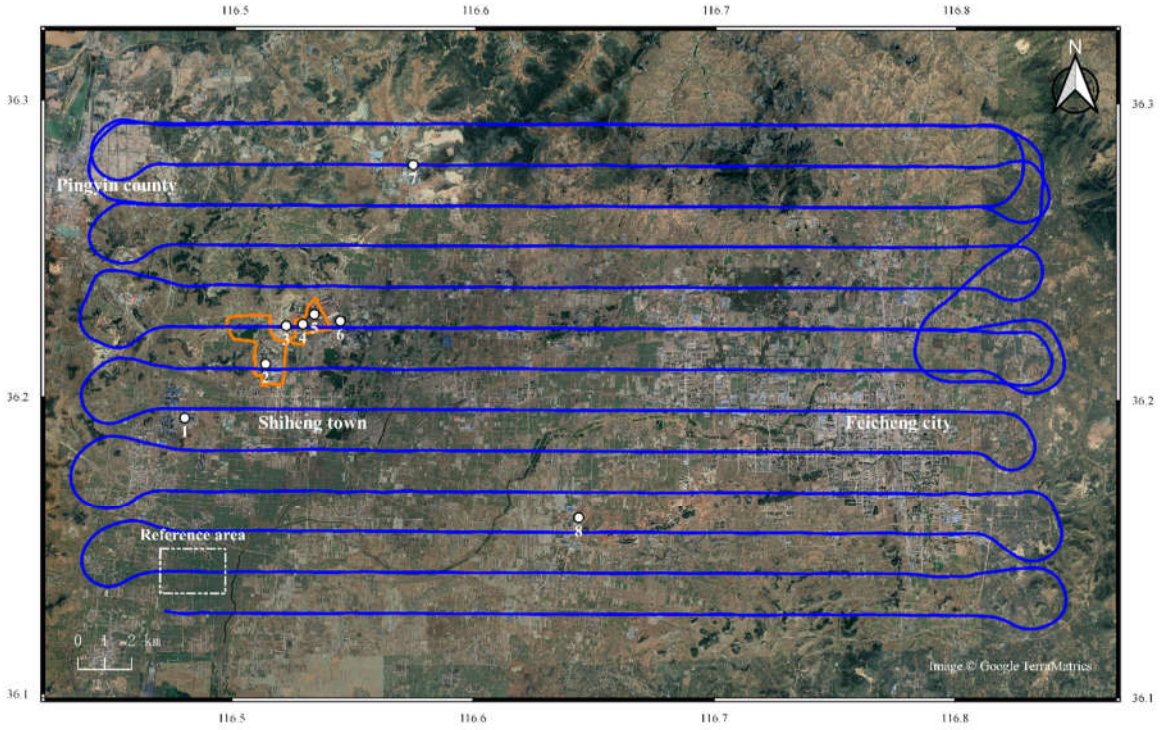

Figure 4. Overview of the Feicheng demonstration flight on 23 June, 2018. Flight lines are shown in blue. Two orange circles represent the routes of mobile DOAS system. White dots numbered from 1 to 8 represent the major emission sources. Number 1: several carbon factories; number 2: a power plant; number 3-6: individual emitters inside the steel factories, while number 4 and 5 are inside the circle of one mobile DOAS route; number 7-8: two cement factories. White dashed box represents the reference area.

19. L 130: replace one "across track" by "along track"

Corrected.

20. L 163: delete the last sentence starting with "the direct output..." this already written in l 152.

Corrected.

21. L 226: Is [28] a reference? Please use the AMT reference style.

Corrected.

22. L 320: "are near downwind of several plumes" replace by "inside the plumes" or "down-wind of the sources"

Corrected.

23. Figure 8: "wavelength 20 nm" looks like a copy-paste-error from figure 9 "SZA 20◦"?

We consolidated Figures 6, 8, and 9 into new Fgure 8, also we corrected this error.

24. Figures 10 and 11: please add the approximate position of the figure 11 in figure 10 and use the same numbers in figure 11.

We updated Figure 11 with same numbers as below:

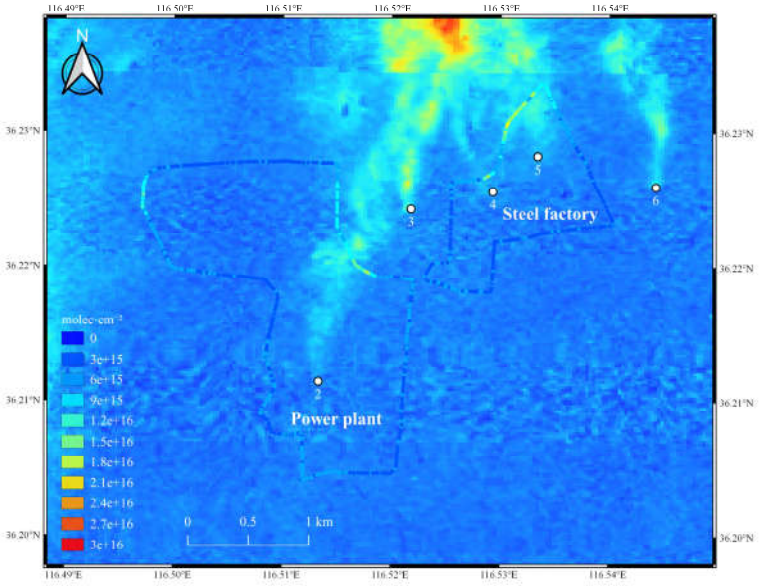

Figure 13. Overview of VCDs retrieved from ground-based mobile DOAS system (circle marks), and VCDs retrieved by UVHIS (background layer), measured on 23 June 2018.

25. In some references there is a layout problem with subscripts like in NO2.

Corrected.

Reference:

An, Z., Huang, R.-J., Zhang, R., Tie, X., Li, G., Cao, J., Zhou, W., Shi, Z., Han, Y., Gu, Z. and Ji, Y.: Severe haze in northern China: A synergy of anthropogenic emissions and atmospheric processes, Proc. Natl. Acad. Sci., 116(18), 8657–8666, doi:10.1073/pnas.1900125116, 2019.

Crippa, M., Guizzardi, D., Muntean, M., Schaaf, E., Dentener, F., van Aardenne, J. A., Monni, S., Doering, U., Olivier, J. G. J., Pagliari, V. and Janssens-Maenhout, G.: Gridded Emissions of Air Pollutants for the period 1970–2012 within EDGAR v4.3.2, preprint, Data, Algorithms, and Models., 2018.

Liu, F., Beirle, S., Zhang, Q., van der A, R. J., Zheng, B., Tong, D. and He, K.: NO_x emission trends over Chinese cities estimated from OMI observations during 2005 to 2015, Atmospheric Chem. Phys., 17(15), 9261–9275, doi:10.5194/acp-17-9261-2017, 2017.

Li, Z. Q., Xu, H., Li, K. T., Li, D. H., Xie, Y. S., Li, L., Zhang, Y., Gu, X. F., Zhao, W., Tian, Q. J., Deng, R. R., Su, X. L., Huang, B., Qiao, Y. L., Cui, W. Y., Hu, Y., Gong, C. L., Wang, Y. Q., Wang, X. F., Wang, J. P., Du, W. B., Pan, Z. Q., Li, Z. Z. and Bu, D.: Comprehensive Study of Optical, Physical, Chemical, and Radiative Properties of Total Columnar Atmospheric Aerosols over China: An Overview of Sun–Sky Radiometer Observation Network (SONET) Measurements, Bull. Am. Meteorol. Soc., 99(4), 739–755, doi:10.1175/BAMS-D-17-0133.1, 2018.

Zhang, C., Liu, C., Hu, Q., Cai, Z., Su, W., Xia, C., Zhu, Y., Wang, S. and Liu, J.: Satellite UV-Vis spectroscopy: implications for air quality trends and their driving forces in China during 2005–2017, Light Sci. Appl., 8(1), 100, doi:10.1038/s41377-019-0210-6, 2019.

Relevant changes:

1. Changed the title.
2. Added a H_2O cross section from HITRAN database in the DOAS analysis.
3. Changed the NO_2 residual in the background spectra to 3×10^{15} molec cm^{-2}, according to TROPOMI tropospheric product of reference area on the same day.
4. Clarified the retrieved NO_2 vertical columns of UVHIS are tropospheric columns.
5. Added enlarged observations over Feicheng city.
6. Added discussion of repeated flight lines and adjacent flight lines.
7. Recalculated the total error of UVHIS tropospheric NO_2 VCDs.
8. Added description of mobile DOAS retrieval method.
9. Added comparison of UVHIS VCDs to mobile measurements that only circled the steel factory.
10. Updated the figures according to suggestions from referees.

~~The Ultraviolet Visible Hyperspectral Imaging Spectrometer (UVHIS), and high-resolution NO_2 mapping from its first airborne observation~~The first high-resolution tropospheric NO_2 observations from the Ultraviolet Visible Hyperspectral Imaging Spectrometer (UVHIS)

Liang Xi [1,2], Fuqi Si [1], Yu Jiang [1], Haijin Zhou [1], Kai Zhan [1], Zhen Chang [1], Xiaohan Qiu [1] and Dongshang Yang [1,2]

[1]Key Laboratory of Environmental Optics and Technology, Anhui Institute of Optics and Fine Mechanics, Chinese Academy of Sciences, Hefei 230031, China
[2] University of Science and Technology of China, Hefei, 230026, Anhui, China

Correspondence to: Fuqi Si (sifuqi@aiofm.ac.cn)

Abstract. We present a novel airborne imaging differential optical absorption spectroscopy (DOAS) instrument: Ultraviolet Visible Hyperspectral Imaging Spectrometer (UVHIS), which is developed for trace gas monitoring and pollution mapping. Within a broad spectral range from 200 to 500 nm, operated in three channels, the spectral resolution of UVHIS is better than 0.5 nm. The optical design of each channel comprises a fore-optics with a field of view (FOV) of 40°, an Offner imaging spectrometer, and a charge-coupled device (CCD) array detector of 1032 × 1072 pixels. A first demonstration flight using UVHIS was undertaken on 23 June 2018, above an approximate 600 km^2 area in Feicheng, China, with a spatial resolution of about 25 × 22 m^2. Measurements of nadir backscattered solar radiation of channel 3 are used to retrieve tropospheric vertical column densities (VCDs) of NO_2 with a mean ~~fitting~~ total error of ~~2.6~~3.0 × 10^{15} molec cm^{-2}. The UVHIS instrument clearly detected several emission plumes transporting from south to north, with a peak value of 3 × 10^{16} molec cm^{-2} in the dominant one. UVHIS NO_2 vertical columns are well correlated with ground-based mobile DOAS observations, with a correlation coefficient of 0.65 for all co-located measurements, a correlation coefficient of 0.86 for co-located measurements that only circled the steel factory, and a slight underestimation for polluted observations. This study demonstrates the capability of UVHIS for NO_2 local emission and transmission monitoring.

1 Introduction

Nitrogen oxides (NO_x), the sum of nitrogen monoxide (NO) and nitrogen dioxide (NO_2), plays a key role in the chemistry of the atmosphere, such as the ozone destruction in the stratosphere (Solomon, 1999), and the secondary aerosol formation in the troposphere (Seinfeld and Pandis, 2016). In the troposphere, despite lightning, soil emissions and other natural processes, the main sources of NO_x are anthropogenic activities like fossil fuel combustion by power plants, factories, and road transportation, especially in the urban and polluted regions. As an indicator of anthropogenic pollution which leads to

negative effects both on the environment and human health, the amounts and spatial distributions of NO_x attract large attention. For example, China becomes one of the largest NO_x emitters in the world due to fast industrialization, meanwhile China is also experiencing a series of severe air pollution problems in recent years (Crippa et al., 2018; An et al., 2019). Therefore measuring NO_x distribution by application of different techniques, would benefit the pollutant emission detection and the air quality trend forecast (Liu et al., 2017; Zhang et al., 2019).

Compared to NO, Nitrogen dioxide (NO_2) is more stable in the atmosphere. Based on the characteristic absorption structures of NO_2 in the ultraviolet-visible spectral range, the differential optical absorption spectroscopy (DOAS) technique has been ~~well~~ applied to retrieve the light path integrated densities from different platforms (Platt and Stutz, 2008). Combining the imaging spectroscopy technique, imaging DOAS instruments were developed in recent years to determine the trace gases temporal variation as well as the two dimensional distribution. Global horizontal distribution of tropospheric NO_2 and other trace gases has been mapped and studied by several space-borne sensors, including SCIAMACHY (Scanning Imaging Absorption Spectrometer for Atmospheric CHartographY; Bovensmann et al., 1999), GOME (Global Ozone Monitoring Experiment; Burrows et al., 1999) ~~and,~~ GOME-2 (Munro et al., 2016), OMI (Ozone Monitoring Instrument; Levelt et al., 2006) and TROPOMI (TROpospheric Ozone Monitoring Instrument; Veefkind et al., 2012). The Environmental trace gases Monitoring Instrument (EIM; Zhao et al., 2018; Cheng et al., 2019; Zhang et al., 2020), as the first designed space-borne trace gas sensor in China, was launched on 9 May 2018, on-board the Chinese GaoFen-5 (GF5) satellite. In terms of spatial resolution, the majority of these space-borne sensors are lower than 10 × 10 km^2, except TROPOMI with a relative higher resolution of 3.5 × 5.5 km^2.

In order to achieve spatial resolution higher than 100 × 100 m^2 ~~for investigation of~~to investigate the spatial distribution in urban areas and individual source emissions, several ~~researches~~ researchers have applied the imaging DOAS instruments on airborne platforms. The airborne imaging DOAS measurement was firstly performed by Heue et al. (2008) over South African Highveld plateau. For the purpose of retrieval of urban NO_2 horizontal distribution, Popp et al. (2012) and Lawrence et al. (2015) performed their measurements separately in Zürich, Switzerland, and Leicester, England. In 2013, an airborne measurement focusing on source emissions was performed in China, over Tianjin, Tangshan and Bohai gulf (Liu et al., 2015). An inter-comparison study of four airborne imaging DOAS instruments over Berlin, Germany, suggests a good agreement between different sensors, and the effectiveness of imaging DOAS to reveal the fine-scale horizontal variability in tropospheric NO_2 in an urban context (Tack et al., 2019).

Here we present a novel airborne imaging DOAS instrument: Ultraviolet Visible Hyperspectral Imaging Spectrometer (UVHIS), designed and developed by Anhui Institute of Optics and Fine Mechanics, Chinese Academy of Sciences (AIOFM, CAS). As a hyperspectral imaging sensor with high spectral and spatial resolution, UVHIS is designed to be operated on aircraft platform for the purpose of atmospheric trace gas measurements and pollution monitoring over large area in a relative short time frame. By using the DOAS technique and geo-referencing, two dimensional spatial distribution of tropospheric NO_2 of its first demonstration flight over Feicheng, China is also presented in this paper.

The organization of this paper is listed as follows: Sect. 2 presents a technical description of UVHIS system, as well as its preflight calibration results. Section 3 introduces the detailed information of its first research flight above Feicheng, China. Section 4 describes the developed algorithm for retrieval and geographical mapping of tropospheric NO_2 vertical column densities from hyperspectral data. Section 5 present the retrieved NO_2 column densities, and Section 6 compares airborne measurements with correlative ground-based data sets from a mobile DOAS system.

2 Instrument Details

1.1 The UVHIS instrument

UVHIS is a hyperspectral instrument measuring nadir backscattered solar radiation in the ultraviolet and visible wavelength region from 200 to 500 nm. The instrument is operated in three channels ~~at wavelength~~with the wavelength ranges of 200-276 nm (channel 1), 276-380 nm (channel 2) and 380-500 nm (channel 3) for minimal stray light effects and highest spectral performance. The main characteristics of UVHIS are summarized in Table 1.

~~As shown in Fig. 1, the optical benches of three channels share a similar design, consisting of~~Figure 1 shows the optical bench of channel 3 and that the other two are similar. The optical design of each channel comprises a telecentric fore-optics, an Offner imaging spectrometer, and a two dimensional charge-coupled device (CCD) array detector. The Offner imaging spectrometer consists of a concave mirror and a convex grating. Backscattered light below the aircraft is collected by a wide-field telescope with a FOV of 40° in the across-track dimension. After passing through a bandpass filter and a 12.5 mm long entrance slit in the focal plane, light is reflected and diffracted by a concave mirror and a convex grating. The dispersed light is imaged onto a frame transfer CCD detector, which consists of 1032 × 1072 individual pixels. For the purpose of alignment and slight adjustment of the spectrometer, only the central 1000 rows of pixel are well illuminated in the across-track dimension. In the wavelength dimension, the image covers central 1024 columns of pixels on the CCD detector while the left and right edge are used to monitor dark current. The spectral sampling and spectral resolution of all three channels can be found in Table 1.

To reduce dark current and improve the signal-to-noise ratio (SNR) of the instrument, the CCD detector is thermally stabilized at −20°C with a temperature stability of ± 0.05°C (Zhang et al., 2017). However, the optical bench is not thermally controlled, because ~~all~~ the instrument is mounted inside the aircraft platform which is ~~basically~~ temperature consistent at 20°C. UVHIS is mounted on a Leica PAV-80 gyro-stabilized platform that provides angular motion compensation. A high-grade Applanix navigation system on-board is used to receive the position (i.e. latitude, longitude, and elevation) and orientation (i.e. pitch, roll, and heading) information, which is required for accurate geo-referencing. The UVHIS instrument telescope collect solar radiation backscattered from the surface and atmosphere through a fused silica window on the bottom of the aircraft. In the case of NO_2 measurement, all observations in this study only use the channel 3.

2.2 Preflight calibration

~~In order to reduce errors in spectral analysis, spectral and radiometric calibration in the laboratory before actual airborne observation is very necessary~~Spectral and radiometric calibration in the laboratory were done prior to flights to reduce errors in spectral analysis.

For radiometric calibration, we use an integrating sphere with a tungsten halogen lamp for channel 2 and channel 3. While for channel 1, a diffuser plate with a Newport xenon lamp is used for a sufficient ultraviolet output. With the help of a well calibrated spectral radiometer to monitor the radiance of calibration system, digital numbers (DNs) from CCD detectors of three channels can be converted to radiance correctly. Uncertainty of absolute radiance calibration of UVHIS is 4.89 % for channel 1, 4.67 % for channel 2 and 4.42 % for channel 3.

The preflight wavelength calibration was also performed in the laboratory, using a mercury–argon lamp and a tunable laser as light sources. We model the slit function of UVHIS using a symmetric Gaussian function. Spectral registration and slit function calibration are achieved by least square fitting of characteristic lines in collected spectra. Table 2 lists the retrieved full-width at half maximums (FWHMs) for channel 3. Figure 2 shows the measured slit functions at 450.504 nm for 9 viewing angles (-20°, -15°, -10°, -5°, 0°, 5°, 10°, 15°, 20°), and respective retrieved slit function shapes using a symmetric Gaussian function. These Gaussian fit results suggest that a symmetric Gaussian function is a reasonable assumption for slit shape in all viewing directions.

3 Research flight

The first demonstration flight above Feicheng city, Shiheng town and neighbouring rural areas was performed on 23 June 2018, aiming at producing tropospheric NO_2 field maps of large area in a relative short time frame. Feicheng is a county-level city in Shandong province, about 410 km away from Beijing. Figure 3 shows the TROPOMI NO_2 tropospheric observation on 23 June, 2018, with the background Google map and the location of Feicheng. The flight area is located on the south bank of the Yellow River, at the western foot of Mount Tai. UVHIS was operated from the Y-5 aircraft at altitude of 3 km above sea level, higher than the height of planetary boundary layer (PBL), with an average aircraft ground speed of 50 m/s. An overview of the observation area and flight lines ~~is~~ are provided in Fig. ~~2~~4. The aircraft took off at local noon from the airfield in Pingyin county, about 19 km northwest of the centre of the field. An area of approximately 600 km^2 was covered in 3 hour, under clean sunny and cloudless conditions with low-speed southerly winds.

Research flight consists of 13 parallel lines in the east-west direction, starting from the lower left corner in Fig. 2. The distance between adjacent lines is 1.5 km, while the swath width of each individual line is about 2.2 km. Gapless coverage between adjacent lines can be guaranteed in this pattern because of the adequate overlap. To validate the NO_2 column densities retrieved from UVHIS by comparison to ground measurements, mobile DOAS measurements were performed inside the research area on the same day. As shown in Fig. ~~5~~4, the measurements of the mobile DOAS system ~~basically~~

circle around the steel factory and the power plant, which are the presumed major emission sources inside the observation area.

~~At a typical flight altitude of 3 km in the Feicheng demonstration flight, the 40° FOV results in a swath width of 2.2 km on the ground.~~ In the condition of spatial binning by 10 pixels across-track, the across-track spatial resolution of the ground pixel ~~in this direction~~ is about 22 m. ~~Meanwhile along track spatial resolution is determined by the product of the detector integration time and the aircraft ground speed, with some variation due to aircraft pitch angle.~~ At typical aircraft ground speed of 50 m/s and integration time of 0.5 s, the along-track spatial resolution of the ground pixel is about 25 m.

4 Data processing chain

The NO_2 tropospheric vertical column density (VCD) retrieval algorithm of UVHIS consists of four major steps. First, some necessary preprocessing procedures are required before any spectral analysis of UVHIS data. Next, UVHIS spectral data after preprocessing are analyzed in a suitable wavelength region by application of the well-established DOAS technique. After that, air mass factors (AMFs) are calculated for every observation based on SCIATRAN radiative transfer model to convert the slant column densities (SCDs) to tropospheric vertical column densities. In the final step, combining with sensor position and orientation information, NO_2 VCDs are geo-referenced and overlaid onto Google satellite map layers.

4.1 Preprocessing

The preprocessing procedure before spectral analysis includes data selection, dark current correction, spatial binning, and in-flight calibration. First, the spectral data acquired during U-turns of aircraft are removed in the processing because of the large and changing orientation angles. Also a threshold of radiance values is set to neglect some over-illuminated ground pixels inside the flight area, which are usually caused by presence of cloud or water mirror reflection. During the entire flight, sun glint on water occurred several times in the southern part of flight area, especially above the river near the reference area. However, cloud was not present due to clean clear-sky weather condition.

The dark current correction is performed based on the measurement at the start of the entire flight by blocking the fore-optics, which is necessary to improve instrument performance and reduce analysis error in DOAS fit.

In order to increase the SNR of the instrument and the sensitivity to NO_2, the raw pixels of imaging DOAS are usually aggregated in across-track direction and ~~across-track~~along-track direction. According to photon statistics when only shot noise is considered, the SNR should rise with square root of number of binned spectra. However, this improved SNR of instrument results a reduction of spatial resolution. In data analysis of Feicheng flight, we use binning of 10 pixels in across-track direction, resulting in a ground pixel size of about 25 × 22 m^2.

Since the wavelength-to-pixel registration and the slit function shape of UVHIS could change compared to laboratory calibration results, in-flight wavelength calibration is essential for the next DOAS analysis. This in-flight wavelength calibration is achieved by fitting the measured spectra to a high-resolution solar reference (Chance and Kurucz, 2010) with

slit function convolution and wavelength shift. The nominal wavelength-to-pixel registration determined in laboratory calibration, is used as initial values in the iteratively fitting procedure for convergence to the optimal solution. The effective shifts and FWHMs of different across-track position are plotted in Fig. ~~3~~5. Results at three wavelengths are shown: blue for 430 nm (the start of the analysis wavelength region), green for 450 nm (the middle of the analysis wavelength region) and red for 470 nm (the end of the analysis wavelength region).

4.2 DOAS analysis

After preprocessing, the observed UVHIS spectra are analysed by the application of QDOAS (Danckaert et al., 2020) software in order to retrieve NO_2 slant column densities. The basic idea of the DOAS approach is to separate broadband signals like surface reflectance and Rayleigh scattering, and narrow-band signals like trace gas molecular absorption. The fitting window is within 430 and 470 nm wavelength region, considered to contain strongly structured NO_2 absorption features, and with low interference of other trace gases such as O_3, O_4, and water vapor. Absorption cross-sections of NO_2 and other trace gases and a synthetic Ring spectrum are simultaneously fitted to the logarithm of the ratio of the observed spectrum and a reference spectrum. These cross sections are made by convolving the high-resolution cross sections with in-flight wavelength calibration results for all across-track positions. Further details of the DOAS analysis setting can be found in Table 3.

For each analysed spectrum, the direct result of the DOAS fit is differential slant column density (dSCD), which is the difference of NO_2 integrated concentration along the effective light path between the studied spectrum and the selected reference spectrum (SCD_{ref}). Reference spectra ~~is~~ were acquired over a clean rural area upwind of the urban and factory areas, in the lower left corner of Fig. ~~2~~4. In the quite homogeneous background area, several spectra were averaged to increase the SNR of the reference spectrum. For the purpose of avoiding across-track biases, a reference spectrum is required for each across-track ~~detector~~ position because of its intrinsic spectral response. Under the assumption that the spatial and temporal variability of the stratospheric NO_2 field is negligible during the test flight, this approach eliminates the stratospheric NO_2 contribution, making the results only sensitive to the tropospheric portion. According to ~~Popp et al. (2012)~~TROPOMI tropospheric NO_2 product of reference area on the same day, the residual NO_2 amount in the background ~~spectrum~~ spectra is estimated to be ~~1~~3 × 10^{15} molec cm^{-2}.

A sample NO_2 DOAS fit result and corresponding residual of UVHIS spectra is illustrated in Fig. ~~4~~6, with a differential slant column density (dSCD) of ~~5.05 ± 0.38 × 10^{16}~~ 4.95 ± 0.34 × 10^{16} molec cm^{-2} and a RMS on the residuals of ~~4.56 × 10^{-3}~~ 4.27 × 10^{-3}. ~~The direct output of the applied DOAS fitting algorithm are dSCDs.~~

4.3 Air mass factor calculations

SCD is the integrated concentration along the effective light path of observation, which is strongly dependent on the viewing geometry and the ~~radiative transfer~~ properties that influence radiative transfer of light through the atmosphere. VCD is the

integrated concentration along a single vertical transect from the Earth's surface to the top of the atmosphere, which is independent of changes in the light path length of SCD.

$$VCD_i = \frac{dSCD_i + SCD_{ref}}{AMF_i} = \frac{dSCD_i + VCD_{ref} \times AMF_{ref}}{AMF_i} \quad (1)$$

As shown in Eq. (1), $dSCD_i$ from the DOAS fit can be converted to tropospheric VCD_i by dividing the AMF_i which accounts for enhancements in the light path (Solomon et al., 1987). In this study, tropospheric NO_2 AMFs have been computed using the SCIATRAN (Rozanov et al., 2014) radiative transfer model (RTM). SCIATRAN model numerically calculates AMFs based on a priori information on the parameters that change effective light path, such as sun and viewing geometry, trace gas and aerosol vertical profiles, surface reflectance ~~etc~~.

4.3.1 Parameters in RTM

(1) During the flight, viewing geometry is retrieved from the orientation information of the aircraft. Solar position defined by the solar zenith angle (SZA) and solar azimuth angle (SAA), as well as relative azimuth angle (RAA) can be calculated, based on the time information, latitude and longitude position of each observation. (2) Since the flight is performed under clear-sky condition, the effect of cloud presence can be neglected in AMF computation. (3) Surface reflectance used in AMF calculation is the product of the Landsat 8 Operational Land Imager (OLI) space-borne instrument (Barsi et al., 2014). Coastal aerosol band (433 to 450 nm) is selected because its bandwidth is relatively narrow, and this band is basically inside the DOAS fitting window (Vermote et al., 2016). (4) Since no accurate trace gas vertical profile is available during the flight, a well-mixed vertical distribution (box profile) of NO_2 in the PBL is assumed. However, accurate PBL height is also unavailable, a typical height of 2 km is a reasonable guess in the case of sunny summer day in mid-latitude area in China. (5) Aerosol optical Depth (AOD) information used in AMF calculation is MODIS AOD product MYD04 at 470 nm on the same day with resampling for every ground UVHIS pixel (Remer et al., 2005), because neither ground-based aerosol measurement is performed, nor any AERONET station data near the flight area ~~is~~ are available. Like the NO_2 profile, the aerosol extinction box profile is constructed from the PBL height and AOD. Single scattering albedo (SSA) is assumed to be 0.93, and asymmetry factor is assumed to be 0.68 for aerosol extinction profile, based on previous studies of typical urban/industrial aerosols (Li et al., 2018).

The Landsat 8 surface reflectance is retrieved through atmospheric correction, using the Second Simulation of the Satellite Signal in the Solar Spectrum Vectorial (6SV) model (Vermote et al., 1997). Since there is no overpass on the same day inside UVHIS research flight area, we choose surface reflectance product on 3 May 2018 considering the sunny weather condition and no cloud presence. The spatial resolution of Landsat is about 30 m, which is slightly larger than UVHIS. A resampling of Landsat 8 surface reflectance product based on nearest neighbour interpolation is performed for every UVHIS ground pixel.

The radiative transfer equation in SCIATRAN is solved in a pseudo-spherical multiple scattering atmosphere, using the scalar discrete ordinate technique. Simulations are performed for sensor altitude of 3 km above sea level, and wavelength of the middle of the NO_2 fitting windows, i.e. 450nm. A NO_2 AMF look-up table (LUT) was computed, with different RTM parameter settings provided in Table 4. For each retrieved dSCD, an AMF was linear interpolated from the LUT based on the sun geometry, viewing geometry, and surface reflectance.

4.3.2 RTM dependence study

1. AMF dependence on the surface reflectance

As shown in Fig. ~~5~~7, a time series of computed AMFs ~~is~~ are plotted for the research flight on 23 June 2018, as well as the corresponding surface reflectance, solar zenith angles, and relative azimuth angles. Other RTM parameters used in the AMF calculations are also provided in Fig. ~~5~~7. Note that only data of nadir observations are plotted for a clearer display, and time gaps between adjacent flight lines can be observed. Despite the greater degree of varieties in viewing and sun geometries, it is obvious that the AMFs strongly depend on the surface reflectance. Previous studies reported in Lawrence et al. (2015), Meier et al. (2017) and Tack et al. (2017) suggest a similar conclusion. A sensitivity test was carried out to investigate the impact of surface reflectance on the AMF calculations, based on SCIATRAN model with varying value of surface reflectance, and fixed value of other parameters. Results of this test ~~is~~ are shown in Fig. ~~6~~8 (a), and indicate that the relation between surface reflectance and AMF is non-linear. Especially when surface reflectance is blow 0.1, AMF increase with surface reflectance rapidly.

Generally speaking, the AMF should be higher in the case of a bright surface reflectance, because more sunlight is reflected from the ground back to atmosphere and then recorded by the airborne sensor. Compared to rural areas, urban and ~~industry~~ industrial areas usually exhibit an enhancement in value of surface reflectance and subsequently an increment of AMF. As shown in Fig. ~~7~~9, the dependency of the AMF on the surface reflectance is very strong. Also a strong variability of surface reflectance and AMF can be observed in these areas. From Fig. 9, we can also observe several slight inconsistencies between UVHIS measured radiance and Landsat 8 surface reflectance product, due to time offset and spatial resolution difference.

~~In this paper we use Landsat 8 surface reflectance product (Vermote et al., 2016) of coastal aerosol band (band 1) as input parameter in AMF calculation. The surface reflectance is retrieved through atmospheric correction, using the Second Simulation of the Satellite Signal in the Solar Spectrum Vectorial (6SV) model (Vermote et al., 1997). Since there is no overpass on the same day inside UVHIS research flight area, we choose surface reflectance product on 3 May 2018 considering the sunny weather condition and no cloud presence. The spatial resolution of Landsat is about 30 m, which is slightly larger than UVHIS. A resampling of Landsat 8 surface reflectance product based on nearest neighbour interpolation is performed for every UVHIS ground pixel.~~

2. AMF dependence on profiles

Based on airborne UVHIS retrieval product, the horizontal distribution of NO_2 can be detected, but the vertical distribution of NO_2 in the atmosphere is not available. The assumptions we made for profile shape of trace gas and aerosol extinction do not consider the effective variability during research flight, which can be expected in an urban area. Focusing on the impact of different profile shapes on the AMF computation, sensitivity tests of two different NO_2 profiles which are closer to ground surface are performed: well-mixed NO_2 box profile of 0.5 and 1 km height. Compared to the box profile of 2 km which is close to the height of PBL, AMFs decrease by an average of 13 % in the case of a box profile of 1.0 km, while AMFs decrease by an average of 22 % in the case of a box profile of 0.5 km.

Depending on the relative position of aerosol and trace gas layer, the optical thickness and scattering properties, aerosols can enhance or reduce the AMF in different ways ~~[28]~~(Meier et al., 2017). If an aerosol layer is located above the majority of the trace gas, ~~the~~ aerosols with high SSA have a shielding effect as less ~~solar~~ scatter light ~~pass~~ passes through the trace gas layer, leading to a shorter light path. On the other hand, if aerosols and the trace gas are present in the same layer, aerosols can lead to multiple scattering effects which extend the light path and result a larger AMF. According to the simulations of a well-mixed aerosol box profile of 2 km and a pure Rayleigh atmosphere, AMFs are slightly higher (about 1 %) compared to pure Rayleigh scenario.

3. AMF dependence on sun and viewing geometries

As can be seen in Fig. ~~5~~7, the effect of sun and viewing geometries on AMFs is very small. Based on a previous study ~~of~~ from Tack et al. (2017), ~~the~~ changing SZA have the greatest effect on AMFs, ~~among other~~in comparison to other sun and viewing geometries. ~~The SZA varies from 12.8° to 37.4° during the 3 h research flight, and AMF at the end of the flight is 10 % larger than at the beginning of the flight when other parameters are assigned to mean value (Fig. 8). Generally, a larger SZA could result a longer light path through the atmosphere and thus a larger AMF.~~ In this study, we also did an AMF dependence analysis on SZAs and VZAs. The SZA varies from 12.8° to 37.4° during the 3 hour research flight, while the VZA ranges from 0° to 30° in most cases. As shown in Fig. 8 (b) and (c), the changes of AMF are less than 10% and 7% respectively, when other parameters are set as mean. Generally, a larger SZA or a larger VZA could result a longer light path through the atmosphere and thus a larger AMF.

4. AMF dependence on the analysis wavelength

The dependence of AMF on analysis wavelength is shown in Fig. 9~~. It is obvious that~~, ~~the~~ The AMF ~~increase~~ increases with the analysis wavelength. This could be explained by Rayleigh scattering characteristics: photons at shorter wavelengths are more likely to be scattered ~~before NO_2 layer~~ than photons at longer wavelengths, leading to the reduced sensitivity to AMF at shorter wavelengths. In the DOAS analysis wavelength window of 430-470 nm, the increase in AMF is about 2 %.

4.4 Geo-referencing and mapping

Accurate geo referencing is essential for emission source locating and data comparison, and can be achieved with sensor position and orientation information recorded by navigation system and IMU on-board. After geo-referencing, the NO_2 VCDs are gridded to combine overlapped adjacent measurements, with a spatial resolution of 0.0003° × 0.0002°. Corresponding to 27 × 22 m^2, the grid size used is slightly larger than the effective spatial resolution of the UVHIS for the purpose of reducing the number of empty grid cells. All VCDs are assigned to a grid cell based on its centre coordinates, and several VCDs in one grid cell are unweighted averaged. The final NO_2 VCD distribution map is plotted over satellite Maps layers in QGIS 3.8 software (QGIS development team, 2020).

5 Results

~~The NO_2 VCD two-dimensional distribution map is shown in Fig. 10 for the research flight on 23 June 2018. In general, with a high performance of UVHIS in spectral and spatial resolution, Figure 10 shows fine-scale NO_2 spatial variability to resolve individual emission sources. The NO_2 distribution is dominated by several exhaust plumes with enhanced NO_2 concentration compared to other areas, which share a largely consistent transportation pattern from south to north. The largest plume with peak values of up to 3×10^{16} molec cm^{-2}, is transporting for at least 9 km downwind inside the observation area. The map is built from 13 overlapped adjacent flight lines, the acquisition time of every track is about 10 minutes. Due to temporal discontinuity of flight lines and dynamic characteristics of NO_2 field, biases can be observed between adjacent flight lines, especially inside the polluted area when wind direction is changed.~~

~~Inside flight area, the predominant NO_2 sources are mainly related to anthropogenic emitters in the northwest part. These sources include a power plant, a steel factory, two cement factories, several carbon factories etc. A strong gradient from south to north is shown in all plumes, consistent with the southerly wind direction. The largest plume originates from an emitter inside a steel factory, which is represented by number 3 in Fig. 10. This dominant plume is transporting at least 9 km from south to north and seems to be continuing outside the flight region. As the plume spreads further north, it becomes much broader. However, it is discontinuous and inhomogeneous in the distribution map, because of time differences among adjacent flight lines, as well as a dynamically changing NO_2 field which is related to wind direction and speed. As shown in Fig. 10, this plume reaches its peak value outside the steel factory, at a small valley about 1 km to the north. This enhanced level of NO_2 may be caused by terrain factor which contributes to the accumulation of pollution gases.~~

~~Number 4 in Fig. 10 represents an isolated exhaust plume originated from another emitter inside the steel factory, with a peak value of 1.4×10^{16} molec cm^{-2}. A weaker plume with peak values of 1.0×10^{16} molec cm^{-2} is also detected by UVHIS, which seems to originate from the power plant. Indicated by number 2 in Fig. 10, this power plant is less than 2 km south of the steel factory. Number 1 in Fig. 10 indicates several carbon factories, which are located on the left side of the flight area. Several plumes with peak values of 1.5×10^{16} molec cm^{-2}, gradually merge together during the transportation downwind.~~

~~Number 5 and Number 6 in Fig. 10 represent two different cement factories. Peak values of these two plumes are 1.5×10^{16} molec cm^{-2} and 1.3×10^{16} molec cm^{-2} respectively.~~

~~The urban areas of Feicheng city and Pingyin county are located on the right side, and on the upper left corner of the flight area respectively. Compared to the industrial areas mentioned above, the pollution levels of the rural and urban areas are much lower due to the lack of contributing sources, ranging from 1 to 4×10^{15} molec cm^{-2}.~~

The tropospheric NO_2 VCD two-dimensional distribution map is shown in Fig. 10 for the research flight on 23 June 2018. With a high performance of UVHIS in spectral and spatial resolution, Figure 10 shows fine-scale NO_2 spatial variability to resolve individual emission sources. In general, the NO_2 distribution is dominated by several exhaust plumes with enhanced NO_2 concentration in the northwest part, which share a transportation pattern from south to north consistent with the wind direction. These sources include a power plant, a steel factory, two cement factories, and several carbon factories. The largest plume with peak values of up to 3×10^{16} molec cm^{-2}, originates from an emitter inside a steel factory (number 3 in Fig. 10). This dominant plume reaches its peak value outside at a small valley about 1 km north of the factory, and is transporting at least 9 km and seems to be continuing outside the flight region. This enhanced level of NO_2 may be caused by terrain factor which contributes to the accumulation of pollution gases.

Number 4 to 6 represent other emitters inside the steel factory. While the exhaust plumes originated from number 4 and 5 merge with the dominant plume, the plume from number 6 transports to north individually with a peak value of 1.4×10^{16} molec cm^{-2}. A weaker plume with peak values of 1.5×10^{16} molec cm^{-2} is also detected by UVHIS, which seems to originate from the power plant. Indicated by number 2 in Fig. 10, this power plant is less than 2 km south of the steel factory. Number 1 in Fig. 10 indicates several carbon factories, which are located on the left side of the flight area. Several plumes with peak values of 1.5×10^{16} molec cm^{-2}, gradually merge together during transportation downwind. Number 7 and Number 8 in Fig. 10 represent two different cement factories. Peak values of these two plumes are 1.5×10^{16} molec cm^{-2} and 1.4×10^{16} molec cm^{-2} respectively.

Compared to the industrial areas mentioned above, the pollution levels of the rural areas are much lower due to the lack of contributing sources, ranging from 2 to 6×10^{15} molec cm^{-2}. The urban area of Feicheng city is located on the right side of the flight area. Figure 11 is an enlarged map of UVHIS NO_2 observations over Feicheng city, with a color scale only extends to 7×10^{15} molec cm^{-2}. Two black lines in Fig. 11 represent the truck roads in this city. The S104 is a provincial highway that crosses Feicheng from north to south, while the S330 crosses Feicheng from east to west. Although lots of noise can be observed in Fig. 11, the NO_2 sources in Feicheng are mainly related to traffic and concentrated along the S104.

Due to temporal discontinuity of flight lines and dynamic characteristics of tropospheric NO_2 field, artefacts can be observed between adjacent flight lines. Figure 12 shows three flight lines that pass through the steel factory, at local time 13:26 (a), 13:32 (c), and 14:57 (b). Panel (a) and (b) represent flight lines that cover the same area with a 1.5 hour time gap, panel (a) and (c) represent adjacent flight lines with a 6 minutes time gap. These flight lines can be divided into three regions: region

A covers no NO_2 source but is affected by carbon factories about 3 km away; region B covers the steel factory as dominant NO_2 source; region C covers no NO_2 source and is not affected by other sources. Compared to region B, there is a large temporal variety of NO_2 VCDs in region A between three flight lines. Region C is temporally consistent with relatively low NO_2 columns. From these observations it may be concluded that largest temporal variability could occur where there is no local NO_2 source but is down-wind of other sources, especially when wind direction is changing.

6 ~~Discussion~~ NO_2 VCD assessment

6.1 Uncertainty analysis

The total uncertainty on the retrieved tropospheric NO_2 VCDs is composed of three parts: (1) uncertainties in the retrieved dSCDs; (2) uncertainties in reference column SCD_{ref}; (3) uncertainties in computed AMFs. Assuming that these uncertainties originating from independent steps are sufficiently uncorrelated, the total uncertainty of tropospheric NO_2 VCD can be quantified as follows:

$$\sigma_{VCD_i} = \sqrt{\left(\frac{\sigma_{dSCD_i}}{AMF_i}\right)^2 + \left(\frac{\sigma_{SCD_{ref}}}{AMF_i}\right)^2 + \left(\frac{SCD_i}{AMF_i^2} \times \sigma_{AMF_i}\right)^2} \quad (2)$$

The first uncertainty source, σ_{dSCDi}, originates from DOAS fit residuals and is a direct output in QDOAS software. This dSCD uncertainty is dominated by shot noise from radiance, electronic noise from the instrument, systematic uncertainties from the cross sections and errors from wavelength calibration. In this study, spatial binning of 10 pixels is performed to reduce this DOAS fit residuals, with a mean slant error of 4.8×10^{15} molec cm^{-2}. Compared to mobile DOAS system, this DOAS fit error is approximately two times larger. Unlikely situation of mobile DOAS system, it becomes a major contributor to the total uncertainty in the case of an airborne sensor, especially in a clean area.

The second uncertainty source, σ_{SCDref}, is caused by the NO_2 residual amount in the reference spectra. ~~Since no direct measurement of the NO_2 column is performed in the reference area, an uncertainty of 100 % is assumed on the estimated NO_2 background amount~~Since we use TROPOMI tropospheric NO_2 product of the clean reference area as background amount, the uncertainty of NO_2 vertical column is estimated to be 1×10^{15} molec cm^{-2} directly from TROPOMI product. ~~This results in an uncertainty of 1.0×10^{15} molec cm^{-2} in the background column~~ Assuming a tropospheric AMF of 2.0 and a tropospheric AMF over the reference spectra of 1.8, this results an uncertainty 9×10^{14} molec cm^{-2} to the tropospheric vertical column.

The third uncertainty source, σ_{AMFi}, derives from uncertainties in the parameter assumptions of radiative transfer model inputs. According to previous studies (Boersma et al., 2004; Pope et al., 2015), it is treated as systematic and depends on the surface albedo, NO_2 profile, aerosol parameters, and cloud fraction. (1) Since the research flight took place under cloudless conditions, cloud fraction is neglected in this case. (2) Results of the dependence tests in Sect. 4.3.2 suggest that the surface

albedo has the most significant effect on the AMF. According to Vermote et al. (2016), the uncertainty of LANDSAT 8 surface reflectance product of band 1 is 0.011. (3) Based on the sensitivity study performed in Sect. 4.3.2, the uncertainty related to the a priori NO_2 profile shape is lower than 22 %. (4) According to the performed simulations of a pure Rayleigh atmosphere, the uncertainty related to aerosol state is estimated to be less than 1 %. (5) Because of the high accuracy of the viewing and sun geometry, and its low impact on the AMF computation revealed in the previous section, the uncertainty related to viewing and sun geometry is expected to be ignorable. Therefore, combining all uncertainty sources in quadrature, a mean relative uncertainty of 24 % on the σ_{AMFi} is obtained.

Based on above discussion, the total uncertainties on the retrieved tropospheric NO_2 VCDs of all observations of the research flight are calculated. They typically range between ~~1~~ 1.5 and ~~5~~ 5.9 × 10^{15} molec cm^{-2}, with a mean value of ~~2.6~~3.0 × 10^{15} molec cm^{-2}.

6.2 Comparison to mobile DOAS measurements

In order to compare UVHIS NO_2 VCDs to ground-based measurements, mobile DOAS observations were performed on 23 June 2018 as well. This mobile DOAS system is composed of a spectrum acquisition unit and a GPS module. The spectrum collection unit consists of a spectrometer, a telescope, an optical fiber, and a workbench. The FOV of this telescope is 0.3°, and its focal length is 69 mm. The spectrometer used is a Maya 2000 Pro spectrometer, with a wavelength range of ~~260~~290-420 nm and a spectral resolution of 0.55 nm. Zenith-sky observations of mobile DOAS are adopted for minimal blocking of buildings and trees in this research. The important properties of the mobile DOAS system and its NO_2 retrieval approach are shown in Table 5.

For better comparison with UVHIS NO_2 observations, assumptions and parameters in tropospheric NO_2 retrieval method for the mobile DOAS were set to the same as the UVHIS. For example, residual amount of NO_2 in reference spectra was set to 3 × 10^{15} molec cm^{-2} with an error of 1 × 10^{15} molec cm^{-2}; mobile DOAS observations only focus on tropospheric portion of NO_2 columns, assumed that the difference of the stratospheric NO_2 columns between observed spectra and reference spectra is negligible; vertical profiles of NO_2 and aerosol extinction, albedo, and aerosol properties in the AMF calculation were set to the same as UVHIS.

Like the uncertainty analysis of UVHIS NO_2 columns, the total uncertainty on the retrieved mobile tropospheric VCD is composed of three parts: (1) the mean uncertainty on dSCD of mobile DOAS is 1.4 × 10^{15} molec cm^{-2}; (2) the uncertainty of reference vertical column is estimated to be 1 × 10^{15} molec cm^{-2}. In the case that the tropospheric AMFs of measured and reference spectra are very close, this part results an uncertainty 1 × 10^{15} molec cm^{-2} to the total uncertainty; (3) the mean relative uncertainty on the AMF calculation is 22 % by square root of the quadratic sum of individual uncertainties like UVHIS. Combining these uncertainties together, the mean total uncertainties on the retrieved tropospheric NO_2 VCD is 2.1 × 10^{15} molec cm^{-2}.

Basically, the route of the mobile DOAS ~~is~~ was designed to encircle the power plant and steel factory which are supposed to be predominant sources. For the comparison, mobile DOAS observations are first gridded to the same sampling of UVHIS pixels, then the VCD of UVHIS NO_2 results is extracted for each co-located mobile measurement. An overview of the mobile DOAS measurements over UVHIS NO_2 layer is shown in Fig. ~~11~~13. ~~It is obvious that~~ NO_2 distributions of mobile DOAS system and UVHIS exhibit similar spatial characteristics, which low values are located in the south of the steel factory and power plant, and high values are ~~near the downwind of several plumes~~inside the plumes.

Figure ~~12~~ 14 (a) shows scatter plots with VCDs retrieved by UVHIS on the x-axis and mobile DOAS VCDs on the y-axis, for all co-located measurements. The corresponding results of linear regression analysis are also provided in Fig. ~~12~~14 (a), with a correlation coefficient of ~~0.65~~0.69, a slope of ~~1.04~~1.30, and an intercept of ~~3.27×10^{13}~~ -9.01×10^{14}. ~~In general, an overestimation of mobile DOAS VCDs of increased value can be observed.~~ The absolute time offset between mobile DOAS and airborne observations can be up to 1 hour, which means that both instruments cannot sample the NO_2 column at certain geolocation simultaneously. As shown in Fig. 14 (b), when only comparing UVHIS VCDs to mobile measurements that circled the steel factory, the correlation coefficient improves to 0.86. In this case, all mobile measurements occurred inside the swath of one flight line of aircraft, and the time offset between instruments shortened to 15 minutes. In general, an underestimation of UVHIS VCDs of increased value can be observed in Fig 14 (a) and (b). Considering the variability in local emissions and meteorology, it is reasonable that the differences between these two instruments exist. Besides, the averaging effect of the area inside an UVHIS pixel can also lead to the underestimation of UVHIS compared to mobile DOAS system.

7 Conclusions

In this paper, we present the newly developed Ultraviolet Visible Hyperspectral Imaging Spectrometer (UVHIS), with a broad spectral region from 200 to 500 nm, and a high spectral resolution better than 0.5 nm. The instrument is operated in three channels at wavelength 200 to 276 nm (channel 1), 276 to 380 nm (channel 2), and 380 to 500 nm (channel 3) for minimal stray light effects and highest spectral performance. The optical design of each channel consists of a fore-optics with a FOV of 40°, an Offner imaging spectrometer, and a CCD array detector of 1032 × 1072 pixels.

Also we present the first tropospheric NO_2 retrieval results from the UVHIS airborne observation in June 2018. The research flight above Feicheng, China, covered an area of about 20 × 30 km^2 within 3 hour, with a high spatial resolution about 25 × 22 m^2. We first retrieve the differential NO_2 slant column densities from nadir observed spectra by application of DOAS technique, to a mean reference spectra over a clean area. Then we convert those NO_2 slant columns to tropospheric vertical columns using air mass factors derived from SCIATRAN model with Landsat 8 surface reflectance product. Total uncertainties of tropospheric NO_2 vertical columns are in range of ~~1~~ 1.5 to ~~5~~ 5.9 × 10^{15} molec cm^{-2}, with a mean value of ~~2.6~~3.0 × 10^{15} molec cm^{-2}.

The two-dimensional distribution map of tropospheric NO_2 VCD demonstrates that UVHIS is adequate for trace gas pollution monitoring over a large area in a relative short time frame. With the high spatial resolution of UVHIS, different local emission sources can be distinguished, fine-scale horizontal variability can be revealed, and trace gas emission and transmission can be understood. For the flight on 23 June 2018, NO_2 distribution is dominated by several exhaust plumes which exhibit same south to north direction of transmission, with a peak value of 3×10^{16} molec cm^{-2} in the dominant plume. Comparisons of UVHIS NO_2 vertical columns to mobile DOAS observations show good agreement overall, with a correlation coefficient of 0.65 for all co-located measurements, and a correlation coefficient of 0.86 for co-located measurements that only circled the steel factory. However, an underestimation of the high NO_2 columns of UVHIS is observed relative to the mobile DOAS measurements.

High-resolution information about the NO_2 horizontal distribution, generated from UVHIS airborne data, is unique and valuable compared to ground-based instruments and space-borne sensors. In future study, UVHIS could be applied in validation of satellite trace gas instruments, and in connection between local point observations, air quality models, and global monitoring from space.

Data availability. The datasets in the present work are available from the corresponding author upon reasonable request.

Author Contributions. Conceptualization, F.S.; methodology, Y.J. and H.Z.; software, Z.C.; validation, X.Q. and D.Y.; formal analysis, L.X.; resources, K.Z.; writing—original draft preparation, L.X.; writing—review and editing, F.S.

Competing Interest. The authors declare no conflict of interest.

Acknowledgments. We would like to thank Thomas Danckaert, Caroline Fayt and Michel Van Roozendael for help on QDOAS software.

Financial support. This research was supported by grants from the National Key Research and Development Program of China (Nos. 2016YFC0200402, 2019YFC0214702).

References

An, Z., Huang, R.-J., Zhang, R., Tie, X., Li, G., Cao, J., Zhou, W., Shi, Z., Han, Y., Gu, Z. and Ji, Y.: Severe haze in northern China: A synergy of anthropogenic emissions and atmospheric processes, Proc. Natl. Acad. Sci., 116(18), 8657–8666, doi:10.1073/pnas.1900125116, 2019.

Barsi, J., Schott, J., Hook, S., Raqueno, N., Markham, B. and Radocinski, R.: Landsat-8 Thermal Infrared Sensor (TIRS) Vicarious Radiometric Calibration, Remote Sens., 6(11), 11607–11626, doi:10.3390/rs61111607, 2014.

Boersma, K. F., Eskes, H. J. and Brinksma, E. J.: Error analysis for tropospheric NO_2 retrieval from space, J. Geophys. Res. Atmospheres, 109(D4), doi:10.1029/2003JD003962, 2004.

Bovensmann, H., Burrows, J. P., Buchwitz, M. and Frerick, J.: SCIAMACHY: Mission Objectives and Measurement Modes, J. ATMOSPHERIC Sci., 56, 24, 1999.

Burrows, J. P., Weber, M., Buchwitz, M., Rozanov, V., TTER-WEIßENMAYER, A. L., Richter, A., Bramstedt, K., Eichmann, K.-U., Eisinger, M. and Perner, D.: The Global Ozone Monitoring Experiment (GOME): Mission Concept and First Scientific Results, J. ATMOSPHERIC Sci., 56, 25, 1999.

Chance, K. and Kurucz, R. L.: An improved high-resolution solar reference spectrum for earth's atmosphere measurements in the ultraviolet, visible, and near infrared, J. Quant. Spectrosc. Radiat. Transf., 111(9), 1289–1295, doi:10.1016/j.jqsrt.2010.01.036, 2010.

Chance, K. V. and Spurr, R. J. D.: Ring effect studies: Rayleigh scattering, including molecular parameters for rotational Raman scattering, and the Fraunhofer spectrum, Appl. Opt., 36(21), 5224, doi:10.1364/AO.36.005224, 1997.

Cheng, L., Tao, J., Valks, P., Yu, C., Liu, S., Wang, Y., Xiong, X., Wang, Z. and Chen, L.: NO_2 Retrieval from the Environmental Trace Gases Monitoring Instrument (EMI): Preliminary Results and Intercomparison with OMI and TROPOMI, Remote Sens., 11(24), 3017, doi:10.3390/rs11243017, 2019.

Crippa, M., Guizzardi, D., Muntean, M., Schaaf, E., Dentener, F., van Aardenne, J. A., Monni, S., Doering, U., Olivier, J. G. J., Pagliari, V. and Janssens-Maenhout, G.: Gridded Emissions of Air Pollutants for the period 1970–2012 within EDGAR v4.3.2, preprint, Data, Algorithms, and Models., 2018.

Danckaert, T., Fayt, C., Roozendael, M. V., Smedt, I. D., Letocart, V., Merlaud, A. and Pinardi, G.: QDOAS Software user manual, [online] Available from: http://uv-vis.aeronomie.be/software/QDOAS/QDOAS_manual.pdf (Accessed 2 June 2020), 2020.

Heue, K.-P., Wagner, T., Broccardo, S. P., Walter, D., Piketh, S. J., Ross, K. E., Beirle, S. and Platt, U.: Direct observation of two dimensional trace gas distributions with an airborne Imaging DOAS instrument, Atmospheric Chem. Phys., 8(22), 6707–6717, doi:10.5194/acp-8-6707-2008, 2008.

Lawrence, J. P., Anand, J. S., Vande Hey, J. D., White, J., Leigh, R. R., Monks, P. S. and Leigh, R. J.: High-resolution measurements from the airborne Atmospheric Nitrogen Dioxide Imager (ANDI), Atmospheric Meas. Tech., 8(11), 4735–4754, doi:10.5194/amt-8-4735-2015, 2015.

Levelt, P. F., van den Oord, G. H. J., Dobber, M. R., Malkki, A., Huib Visser, Johan de Vries, Stammes, P., Lundell, J. O. V. and Saari, H.: The ozone monitoring instrument, IEEE Trans. Geosci. Remote Sens., 44(5), 1093–1101, doi:10.1109/TGRS.2006.872333, 2006.

Li, Z. Q., Xu, H., Li, K. T., Li, D. H., Xie, Y. S., Li, L., Zhang, Y., Gu, X. F., Zhao, W., Tian, Q. J., Deng, R. R., Su, X. L., Huang, B., Qiao, Y. L., Cui, W. Y., Hu, Y., Gong, C. L., Wang, Y. Q., Wang, X. F., Wang, J. P., Du, W. B., Pan, Z. Q., Li, Z. Z. and Bu, D.: Comprehensive Study of Optical, Physical, Chemical, and Radiative Properties of Total Columnar Atmospheric Aerosols over China: An Overview of Sun–Sky Radiometer Observation Network (SONET) Measurements, Bull. Am. Meteorol. Soc., 99(4), 739–755, doi:10.1175/BAMS-D-17-0133.1, 2018.

Liu, F., Beirle, S., Zhang, Q., van der A, R. J., Zheng, B., Tong, D. and He, K.: NO_x emission trends over Chinese cities estimated from OMI observations during 2005 to 2015, Atmospheric Chem. Phys., 17(15), 9261–9275, doi:10.5194/acp-17-9261-2017, 2017.

Liu, J., Si, F., Zhou, H., Zhao, M., Dou, K., Wang, Y. and Liu, W.: Observation of two-dimensional distributions of NO_2 with airborne imaging DOAS technology, Acta Phys. Sin., 64(3), 034217, doi:10.7498/aps.64.034217, 2015.

Meier, A. C., Schönhardt, A., Bösch, T., Richter, A., Seyler, A., Ruhtz, T., Constantin, D.-E., Shaiganfar, R., Wagner, T., Merlaud, A., Van Roozendael, M., Belegante, L., Nicolae, D., Georgescu, L. and Burrows, J. P.: High-resolution airborne imaging DOAS measurements of NO_2 above Bucharest during AROMAT, Atmospheric Meas. Tech., 10(5), 1831–1857, doi:10.5194/amt-10-1831-2017, 2017.

Munro, R., Lang, R., Klaes, D., Poli, G., Retscher, C., Lindstrot, R., Huckle, R., Lacan, A., Grzegorski, M., Holdak, A., Kokhanovsky, A., Livschitz, J. and Eisinger, M.: The GOME-2 instrument on the Metop series of satellites: instrument design, calibration, and level 1 data processing – an overview, Atmospheric Meas. Tech., 9(3), 1279–1301, doi:10.5194/amt-9-1279-2016, 2016.

Platt, U. and Stutz, J.: Differential Optical Absorption Spectroscopy: Principles and Applications, Springer-Verlag, Berlin, Germany., 2008.

Pope, R. J., Chipperfield, M. P., Savage, N. H., Ordóñez, C., Neal, L. S., Lee, L. A., Dhomse, S. S., Richards, N. A. D. and Keslake, T. D.: Evaluation of a regional air quality model using satellite column NO_2 treatment of observation errors and model boundary conditions and emissions, Atmospheric Chem. Phys., 15(10), 5611–5626, doi:10.5194/acp-15-5611-2015, 2015.

Popp, C., Brunner, D., Damm, A., Van Roozendael, M., Fayt, C. and Buchmann, B.: High-resolution NO_2 remote sensing from the Airborne Prism EXperiment (APEX) imaging spectrometer, Atmospheric Meas. Tech., 5(9), 2211–2225, doi:10.5194/amt-5-2211-2012, 2012.

QGIS development team: QGIS Geographic Information System, Open Source Geospatial Foundation, QGIS Geogr. Inf. Syst. Open Source Geospatial Found. [online] Available from: https://www.qgis.org/en/site/ (Accessed 2 June 2020), 2020.

Remer, L. A., Kaufman, Y. J., Tanré, D., Mattoo, S., Chu, D. A., Martins, J. V., Li, R.-R., Ichoku, C., Levy, R. C., Kleidman, R. G., Eck, T. F., Vermote, E. and Holben, B. N.: The MODIS Aerosol Algorithm, Products, and Validation, J. Atmospheric Sci., 62(4), 947–973, doi:10.1175/JAS3385.1, 2005.

Rothman, L. S., Gordon, I. E., Babikov, Y., Barbe, A., Chris Benner, D., Bernath, P. F., Birk, M., Bizzocchi, L., Boudon, V., Brown, L. R., Campargue, A., Chance, K., Cohen, E. A., Coudert, L. H., Devi, V. M., Drouin, B. J., Fayt, A., Flaud, J.-M., Gamache, R. R., Harrison, J. J., Hartmann, J.-M., Hill, C., Hodges, J. T., Jacquemart, D., Jolly, A., Lamouroux, J., Le Roy, R. J., Li, G., Long, D. A., Lyulin, O. M., Mackie, C. J., Massie, S. T., Mikhailenko, S., Müller, H. S. P., Naumenko, O. V., Nikitin, A. V., Orphal, J., Perevalov, V., Perrin, A., Polovtseva, E. R., Richard, C., Smith, M. A. H., Starikova, E., Sung, K., Tashkun, S., Tennyson, J., Toon, G. C., Tyuterev, Vl. G. and Wagner, G.: The HITRAN2012 molecular spectroscopic database, J. Quant. Spectrosc. Radiat. Transf., 130, 4–50, doi:10.1016/j.jqsrt.2013.07.002, 2013.

Rozanov, V. V., Rozanov, A. V., Kokhanovsky, A. A. and Burrows, J. P.: Radiative transfer through terrestrial atmosphere and ocean: Software package SCIATRAN, J. Quant. Spectrosc. Radiat. Transf., 133, 13–71, doi:10.1016/j.jqsrt.2013.07.004, 2014.

Seinfeld, J. H. and Pandis, S. N.: Atmospheric chemistry and physics: from air pollution to climate change, Third edition., John Wiley & Sons, Hoboken, New Jersey., 2016.

Serdyuchenko, A., Gorshelev, V., Weber, M., Chehade, W. and Burrows, J. P.: High spectral resolution ozone absorption cross-sections - Part 2: Temperature dependence, Atmospheric Meas. Tech., 7(2), 625–636, doi:10.5194/amt-7-625-2014, 2014.

Solomon, S.: Stratospheric ozone depletion: A review of concepts and history, Rev. Geophys., 37(3), 275–316, doi:10.1029/1999RG900008, 1999.

Solomon, S., Schmeltekopf, A. L. and Sanders, R. W.: On the interpretation of zenith sky absorption measurements, J. Geophys. Res., 92(D7), 8311, doi:10.1029/JD092iD07p08311, 1987.

Tack, F., Merlaud, A., Iordache, M.-D., Danckaert, T., Yu, H., Fayt, C., Meuleman, K., Deutsch, F., Fierens, F. and Van Roozendael, M.: High-resolution mapping of the NO_2 spatial distribution over Belgian urban areas based on airborne APEX remote sensing, Atmospheric Meas. Tech., 10(5), 1665–1688, doi:10.5194/amt-10-1665-2017, 2017.

Tack, F., Merlaud, A., Meier, A. C., Vlemmix, T., Ruhtz, T., Iordache, M.-D., Ge, X., van der Wal, L., Schuettemeyer, D., Ardelean, M., Calcan, A., Constantin, D., Schönhardt, A., Meuleman, K., Richter, A. and Van Roozendael, M.: Intercomparison of four airborne imaging DOAS systems for tropospheric NO_2 mapping – the AROMAPEX campaign, Atmospheric Meas. Tech., 12(1), 211–236, doi:10.5194/amt-12-211-2019, 2019.

Thalman, R. and Volkamer, R.: Temperature dependent absorption cross-sections of O_2–O_2 collision pairs between 340 and 630 nm and at atmospherically relevant pressure, Phys. Chem. Chem. Phys., 15(37), 15371, doi:10.1039/c3cp50968k, 2013.

Vandaele, A. C., Hermans, C., Simon, P. C., Carleer, M., Colin, R., Fally, S., Mérienne, M. F., Jenouvrier, A. and Coquart, B.: Measurements of the NO_2 absorption cross-section from 42 000 cm^{-1} to 10 000 cm^{-1} (238–1000 nm) at 220 K and 294 K, J. Quant. Spectrosc. Radiat. Transf., 59(3–5), 171–184, doi:10.1016/S0022-4073(97)00168-4, 1998.

Veefkind, J. P., Aben, I., McMullan, K., Förster, H., de Vries, J., Otter, G., Claas, J., Eskes, H. J., de Haan, J. F., Kleipool, Q., van Weele, M., Hasekamp, O., Hoogeveen, R., Landgraf, J., Snel, R., Tol, P., Ingmann, P., Voors, R., Kruizinga, B., Vink, R., Visser, H. and Levelt, P. F.: TROPOMI on the ESA Sentinel-5 Precursor: A GMES mission for global observations of the atmospheric composition for climate, air quality and ozone layer applications, Remote Sens. Environ., 120, 70–83, doi:10.1016/j.rse.2011.09.027, 2012.

Vermote, E., Justice, C., Claverie, M. and Franch, B.: Preliminary analysis of the performance of the Landsat 8/OLI land surface reflectance product, Remote Sens. Environ., 11, 2016.

Vermote, E. F., Tanre, D., Deuze, J. L., Herman, M. and Morcette, J.-J.: Second Simulation of the Satellite Signal in the Solar Spectrum, 6S: an overview, IEEE Trans. Geosci. Remote Sens., 35(3), 675–686, doi:10.1109/36.581987, 1997.

Zhang, C., Liu, C., Hu, Q., Cai, Z., Su, W., Xia, C., Zhu, Y., Wang, S. and Liu, J.: Satellite UV-Vis spectroscopy: implications for air quality trends and their driving forces in China during 2005–2017, Light Sci. Appl., 8(1), 100, doi:10.1038/s41377-019-0210-6, 2019.

Zhang, C., Liu, C., Chan, K. L., Hu, Q., Liu, H., Li, B., Xing, C., Tan, W., Zhou, H., Si, F. and Liu, J.: First observation of tropospheric nitrogen dioxide from the Environmental Trace Gases Monitoring Instrument onboard the GaoFen-5 satellite, Light Sci. Appl., 9(1), 66, doi:10.1038/s41377-020-0306-z, 2020.

Zhang, Q., Huang, S., Zhao, X., Si, F., Zhou, H., Wang, Y. and Liu, W.: The Design and Implementation of CCD Refrigeration System of Imaging Spectrometer, Acta Photonica Sin., 46(3), 0311004, 2017.

Zhao, M. J., Si, F. Q., Zhou, H. J., Wang, S. M., Jiang, Y. and Liu, W. Q.: Preflight calibration of the Chinese Environmental Trace Gases Monitoring Instrument (EMI), Atmospheric Meas. Tech., 11(9), 5403–5419, doi:10.5194/amt-11-5403-2018, 2018.

Table 1: UVHIS instrument characteristics of three channels.

Characteristic	Channel 1	Channel 2	Channel 3
Wavelength range	200-276 nm	276-380 nm	380-500 nm
Spectral sampling	0.074 nm	0.10 nm	0.12 nm
Spectral resolution	0.34 nm	0.46 nm	0.49 nm
FOV	40°	40°	40°
Focal length	18 mm	18 mm	18 mm
Across-track angular resolution	0.5 mrad	0.5 mrad	0.5 mrad
f-number	3.4	3.6	3.6
Detector size	1032 × 1072	1032 × 1072	1032 × 1072

Table 2. Preflight wavelength calibration results (FWHMs) of UVHIS channel 3 for 9 viewing angles. Light sources used in the calibration are a mercury-argon lamp and a tunable laser. Slit function shapes are retrieved by least square fitting of characteristic spectral lines, using a symmetric Gaussian function.

FOV	379.887 nm	404.656 nm	450.504 nm	500.566 nm
-20°	0.35 nm	0.35 nm	0.39 nm	0.50 nm
-15°	0.33 nm	0.31 nm	0.33 nm	0.43 nm
-10°	0.31 nm	0.29 nm	0.29 nm	0.41 nm
-5°	0.31 nm	0.30 nm	0.29 nm	0.34 nm
0°	0.31 nm	0.32 nm	0.30 nm	0.30 nm
5°	0.34 nm	0.36 nm	0.34 nm	0.30 nm
10°	0.38 nm	0.39 nm	0.38 nm	0.32 nm
15°	0.40 nm	0.44 nm	0.42 nm	0.35 nm
20°	0.45 nm	0.46 nm	0.47 nm	0.38 nm

Table 3. Main analysis parameters and absorption cross sections for NO_2 DOAS retrieval.

Parameter	Settings
Wavelength calibration	Solar atlas, (Chance and Kurucz, 2010)
Fitting interval	430-470 nm
Cross sections	
NO_2	298 K, Vandaele et al. (1998)
O_3	223 K, Serdyuchenko et al. (2014)
O_4	293 K, Thalman and Volkamer (2013)
H_2O	293 K, Rothman et al. (2013)
Ring effect	Chance and Spurr (1997)
Polynomial term	Order 5
Intensity offset	Order 1

Table 4. Overview of the input parameters in the SCIATRAN RTM, characterizing the AMF LUT.

RTM Parameter	Grid settings
Wavelength	450 nm
Sensor altitude	3 km
Surface reflectance	0.01-0.4 (steps of 0.01)
Solar zenith angle	10-40° (steps of 10°)
Viewing zenith angle	0-40° (steps of 10°)
Relative azimuth angle	0-180° (steps of 30°)
Aerosol optical depth	0-1 (steps of 0.1)
Aerosol extinction profile	Box of 2.0 km
NO_2 profile	Box of 2.0 km

Table 5. Properties of the mobile DOAS system and its NO_2 fit.

Parameter	Settings
Elevation angle	zenith
Fitting interval	356-376 nm
Wavelength calibration	Mercury lamp
Cross sections	
NO_2	298 K, Vandaele et al. (1998)
O_3	223 K, Serdyuchenko et al. (2014)
O_4	293 K, Thalman and Volkamer (2013)
Ring effect	Chance and Spurr (1997)
Polynomial term	Order 5
Intensity offset	Order 1

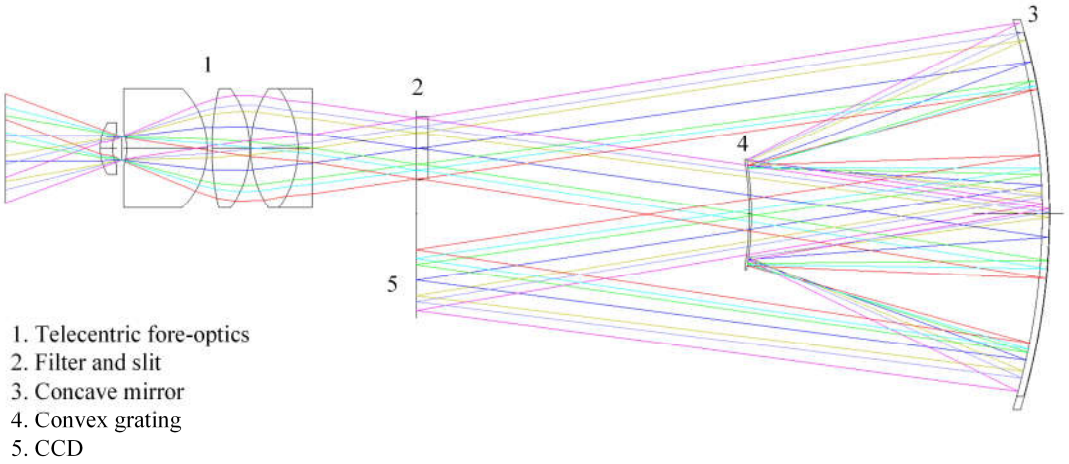

Figure 1. Optical layout of the UVHIS channel 3. Optical design of channel 1 and channel 2 is similar.

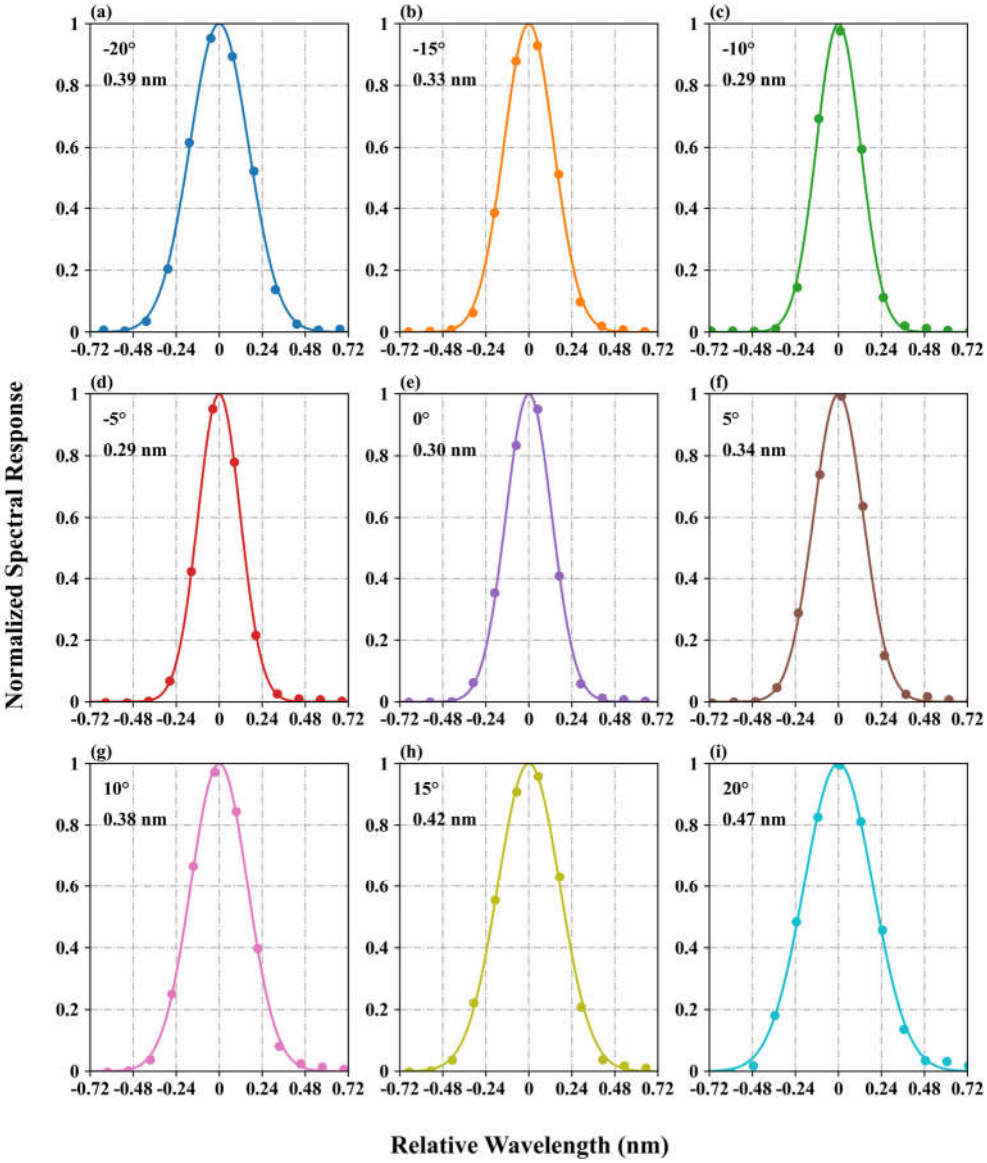

Figure 2. Measured slit functions (dots) at 450.504 nm and retrieved slit function shapes (lines) using a symmetric Gaussian function for 9 viewing angles.

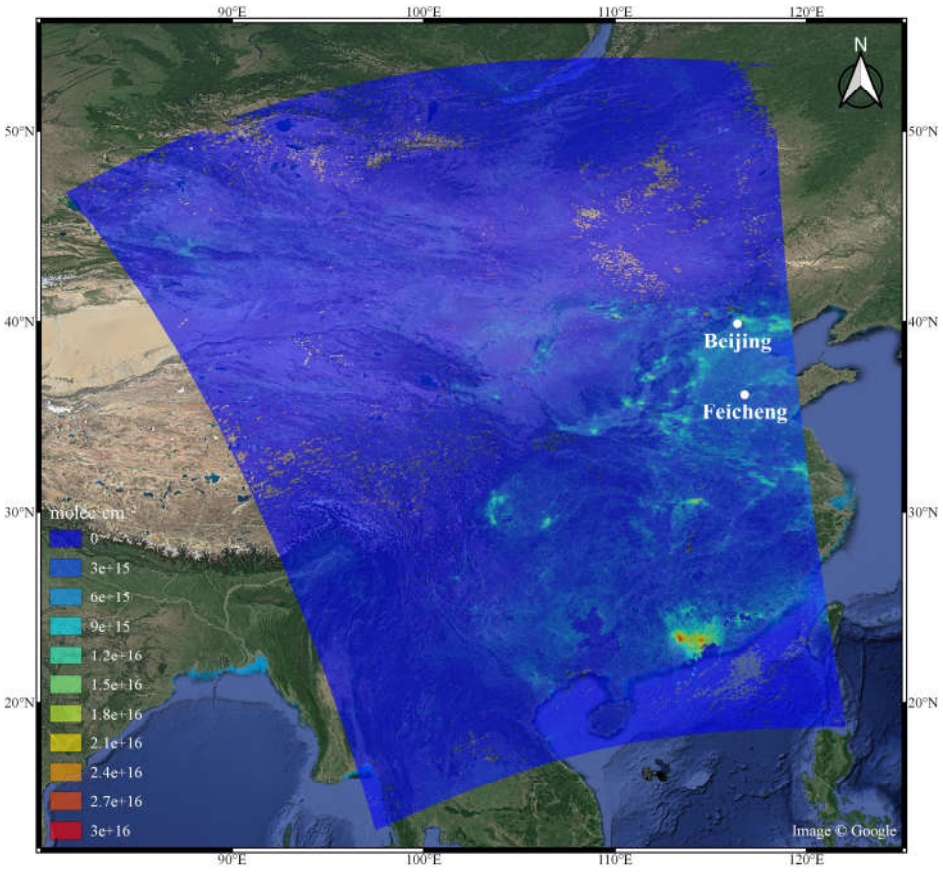

Figure 3. TROPOMI observation of tropospheric NO_2 over China on 23 June, 2018. The location of UVHIS flight (Feicheng city) is also plotted in the map.

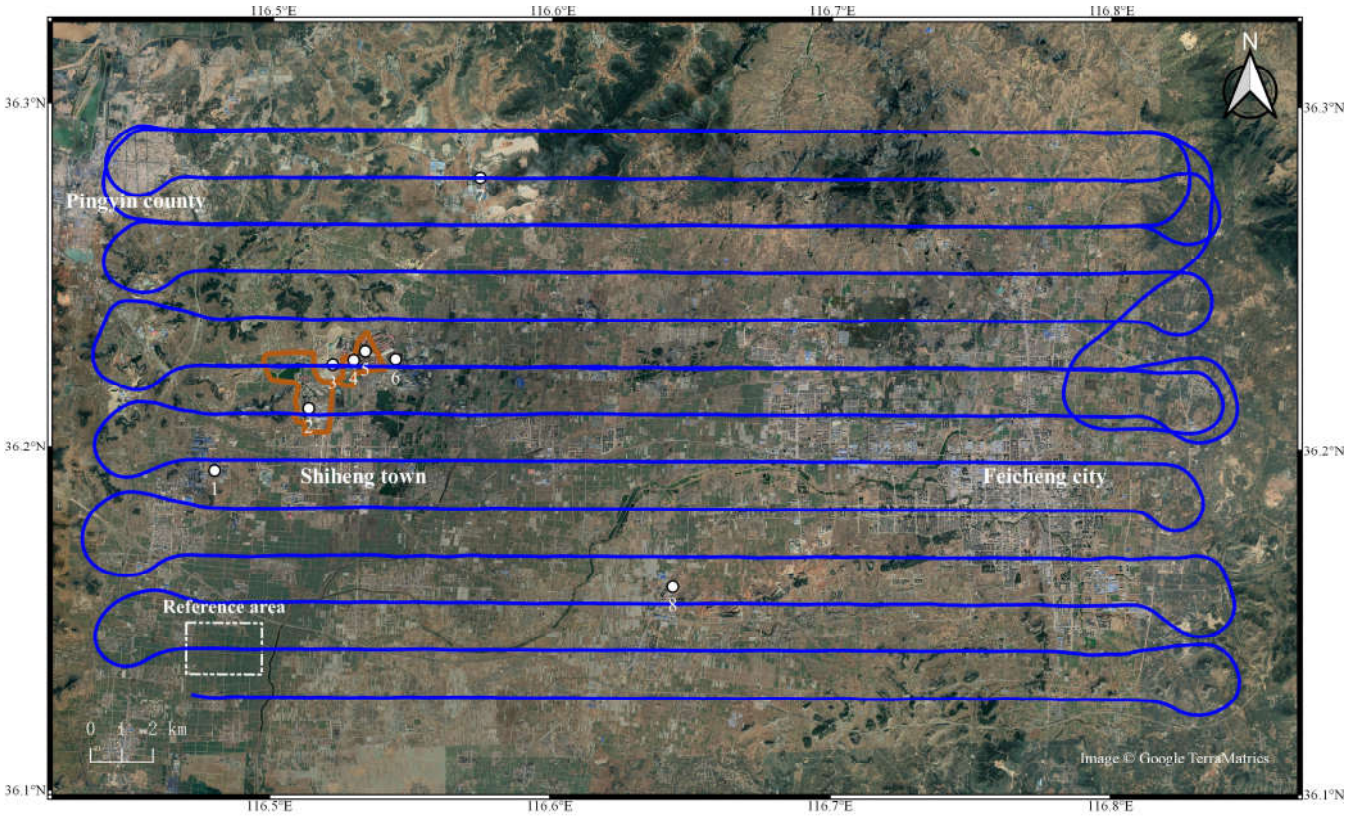

Figure 4. Overview of the Feicheng demonstration flight on 23 June, 2018. Flight lines are shown in blue. Two orange circles represent the routes of mobile DOAS system. White dots numbered from 1 to 8 represent the major emission sources. Number 1: several carbon factories; number 2: a power plant; number 3-6: individual emitters inside the steel factories, while number 4 and 5 are inside the circle of one mobile DOAS route; number 7-8: two cement factories. White dashed box represents the reference area.

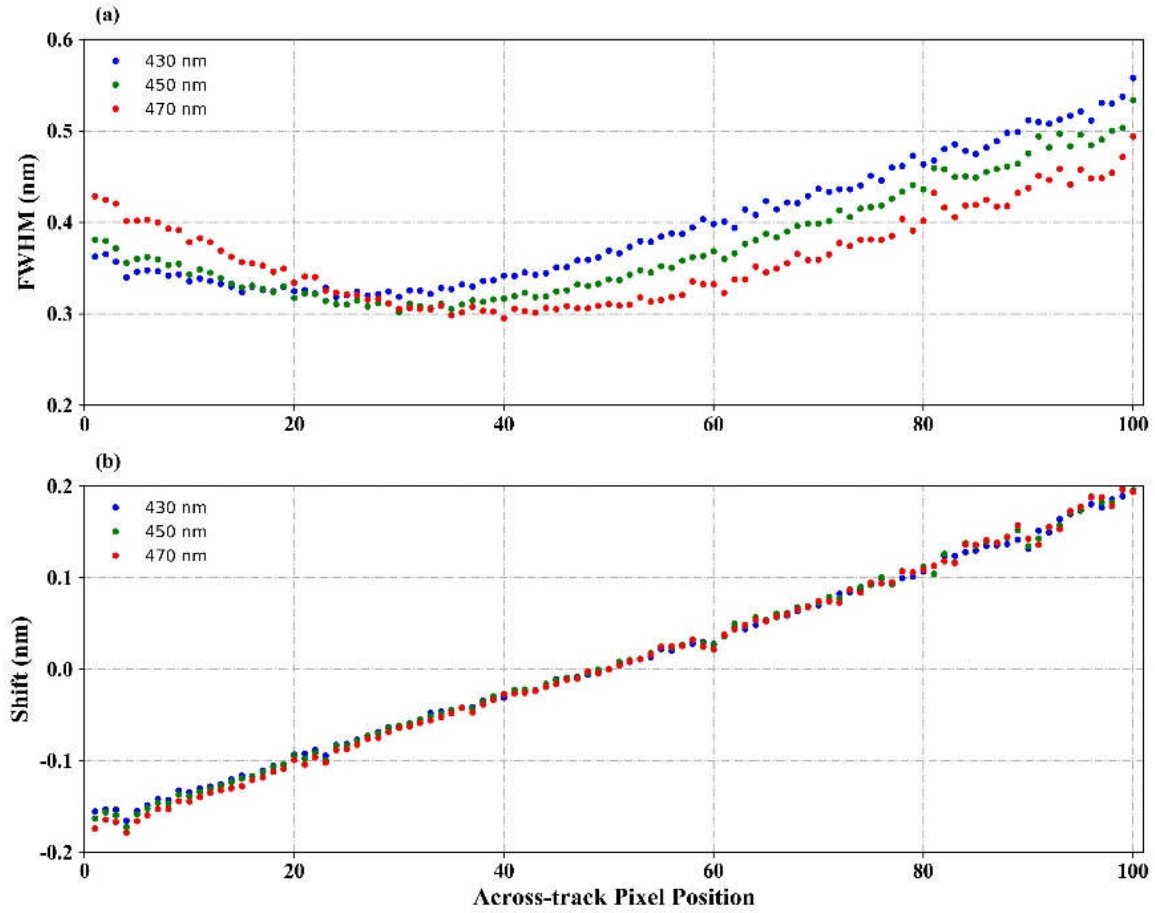

Figure 5. In-flight spectral calibration: (**a**) the spectral resolution (FWHM); (**b**) the spectral shift on different across-track position. Results at three wavelengths are plotted: blue for 430 nm, green for 450 nm and red for 470 nm.

1390

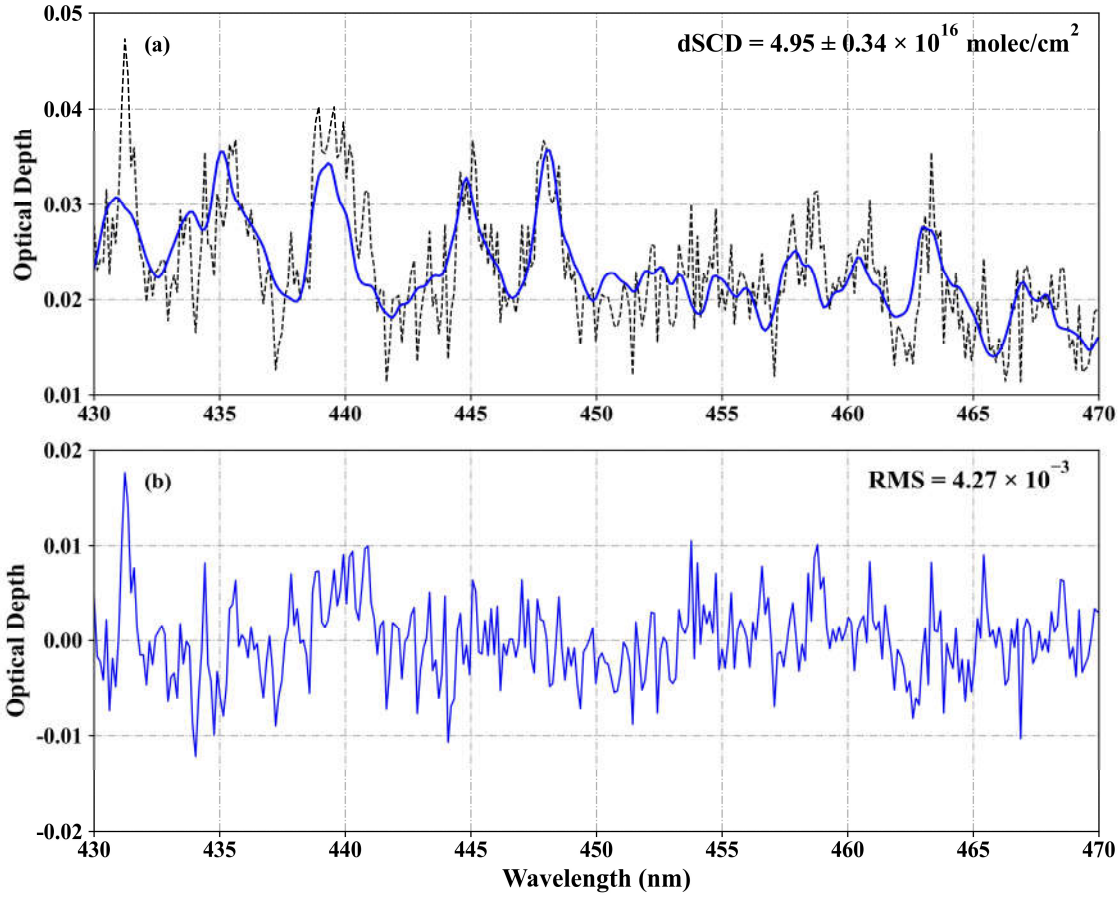

Figure 6. Sample DOAS fit result for NO_2: (**a**) observed (black dashed line) and fitted (blue line) optical depths from measured spectra; (**b**) the remaining residuals of DOAS fit.

1395

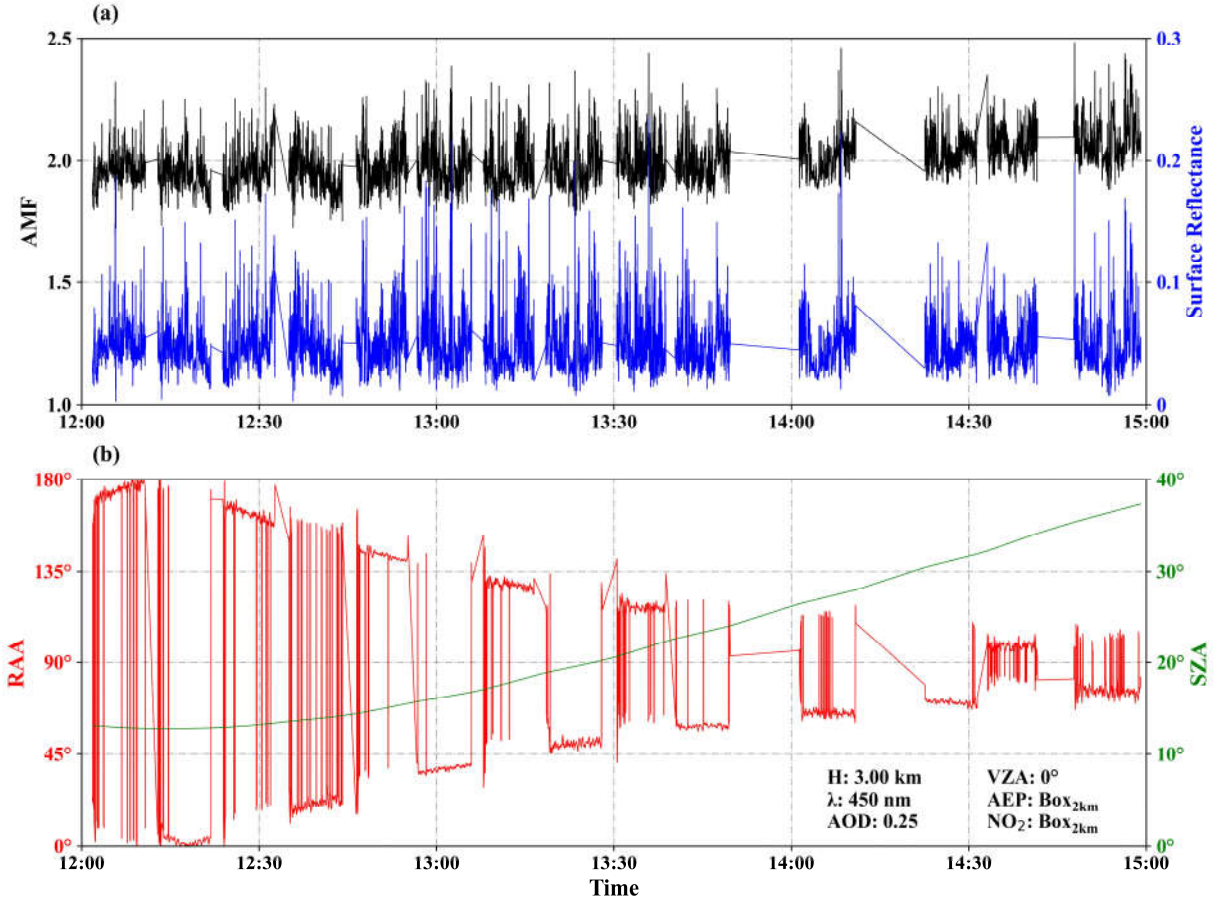

Figure 7. Time series of NO_2 AMF compared with **(a)** surface reflectance; **(b)** SZA and RAA for the research flight on 23 June 2018, computed with SCIATRAN model based on the RTM parameters from the UVHIS instrument. Only data of the nadir observations in each flight line are plotted.

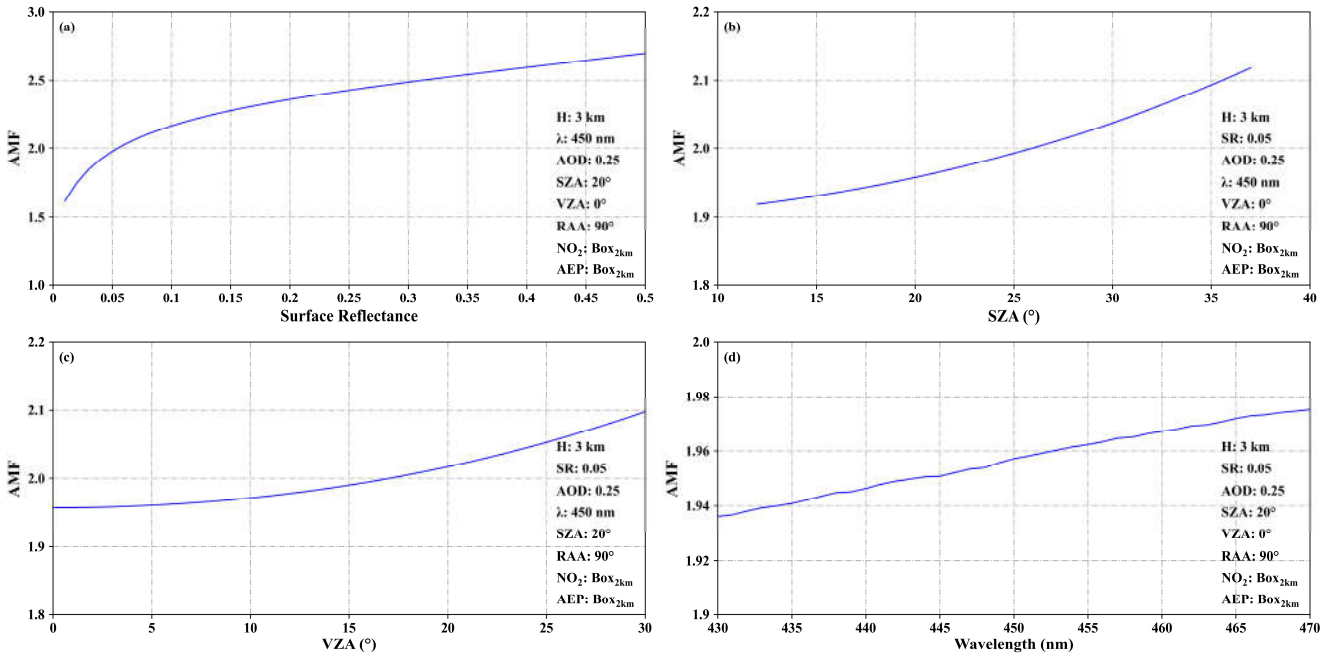

Figure 8. AMF dependence analysis results (a): on the surface reflectance; (b): on the SZAs; (c): on the VZAs; (d): on the wavelength.

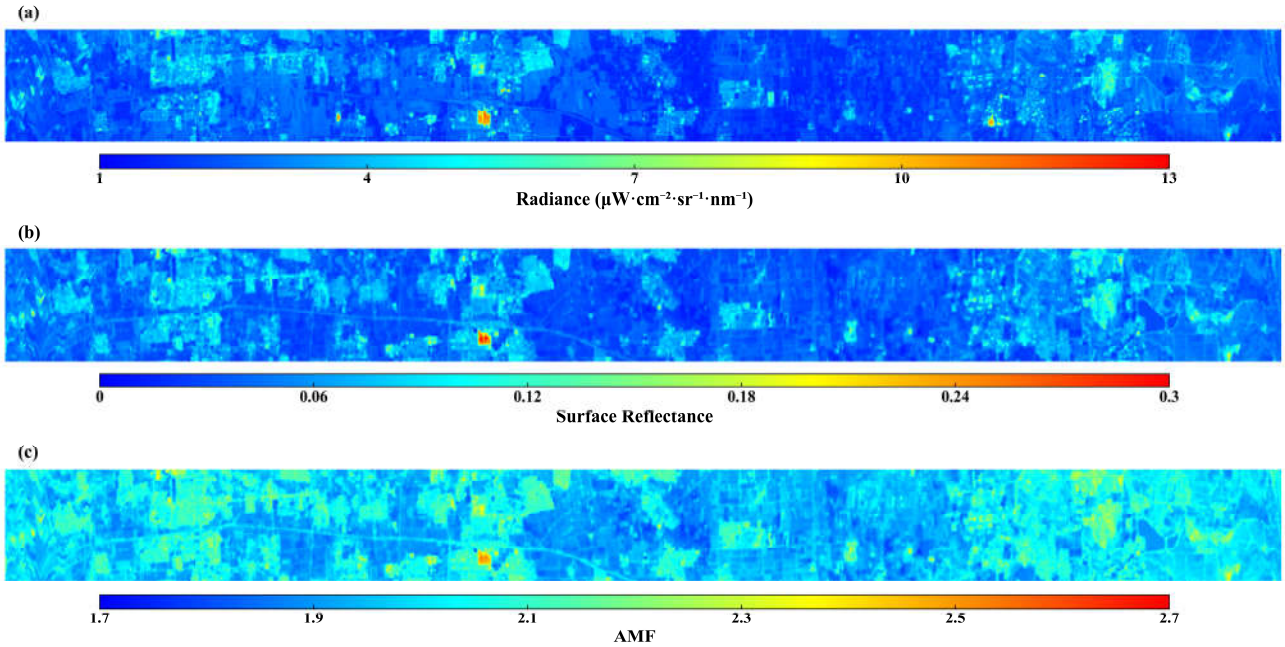

Figure 9. (a) ~~Surface reflectance~~UVHIS Measured radiance; **(b)** ~~computed AMFs~~Landsat 8 Surface reflectance; (c) computed AMFs, for one flight line of the Feicheng data set. A strong dependency of the AMF on the surface reflectance can be observed.

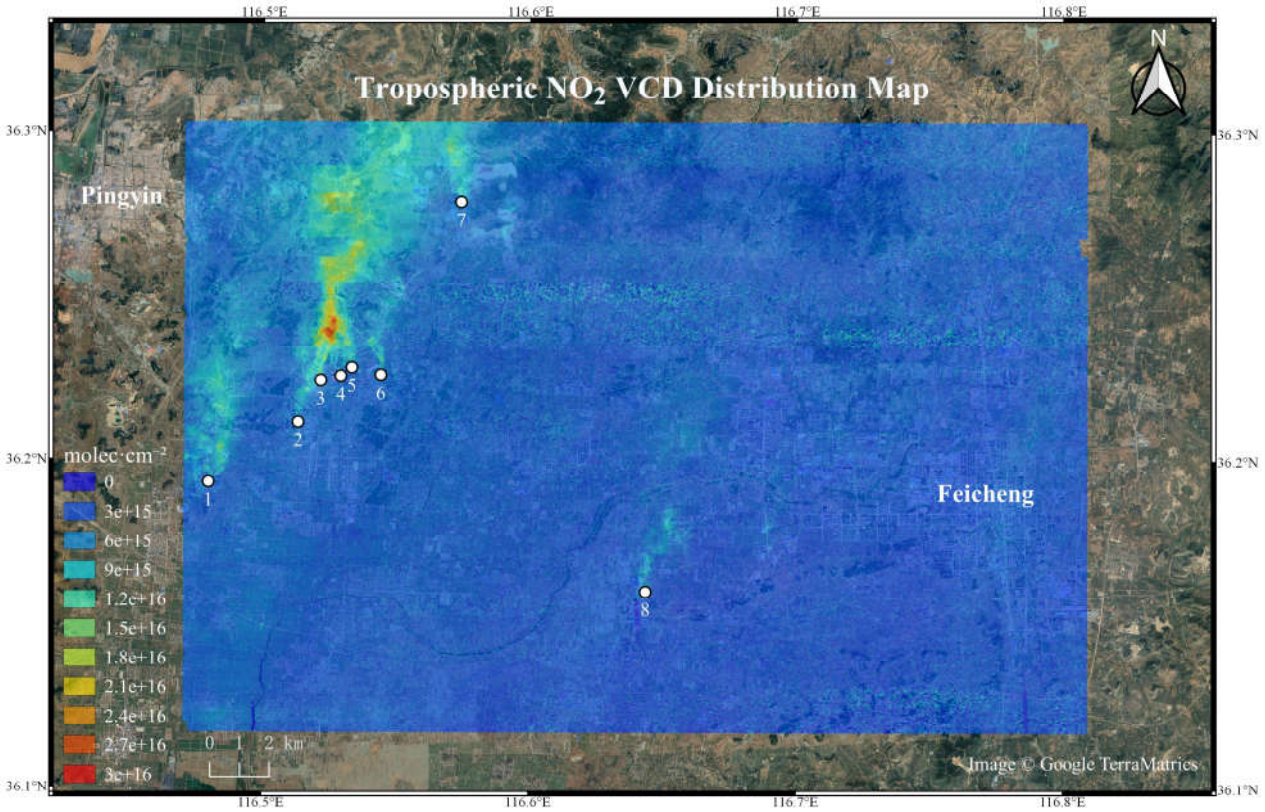

Figure 10. Tropospheric NO_2 VCD map retrieved from UVHIS over Feicheng on 23 June 2018. The major contributing NO_2 emission sources are indicated by number 1 to ~~6~~8.

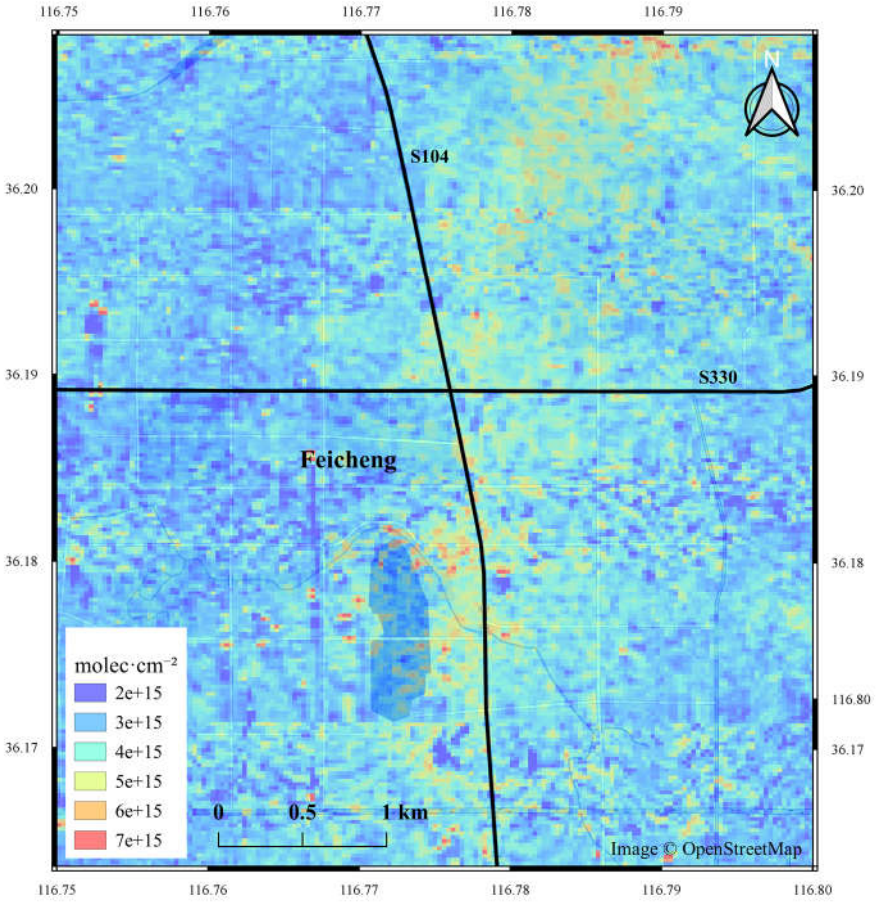

Figure 11. Enlargement of UVHIS NO_2 VCD map over Feicheng city with a color scale only extends to 7×10^{15} molec cm^{-2}. Two black lines in the map represent two truck roads that cross Feicheng city: S104, and S330.

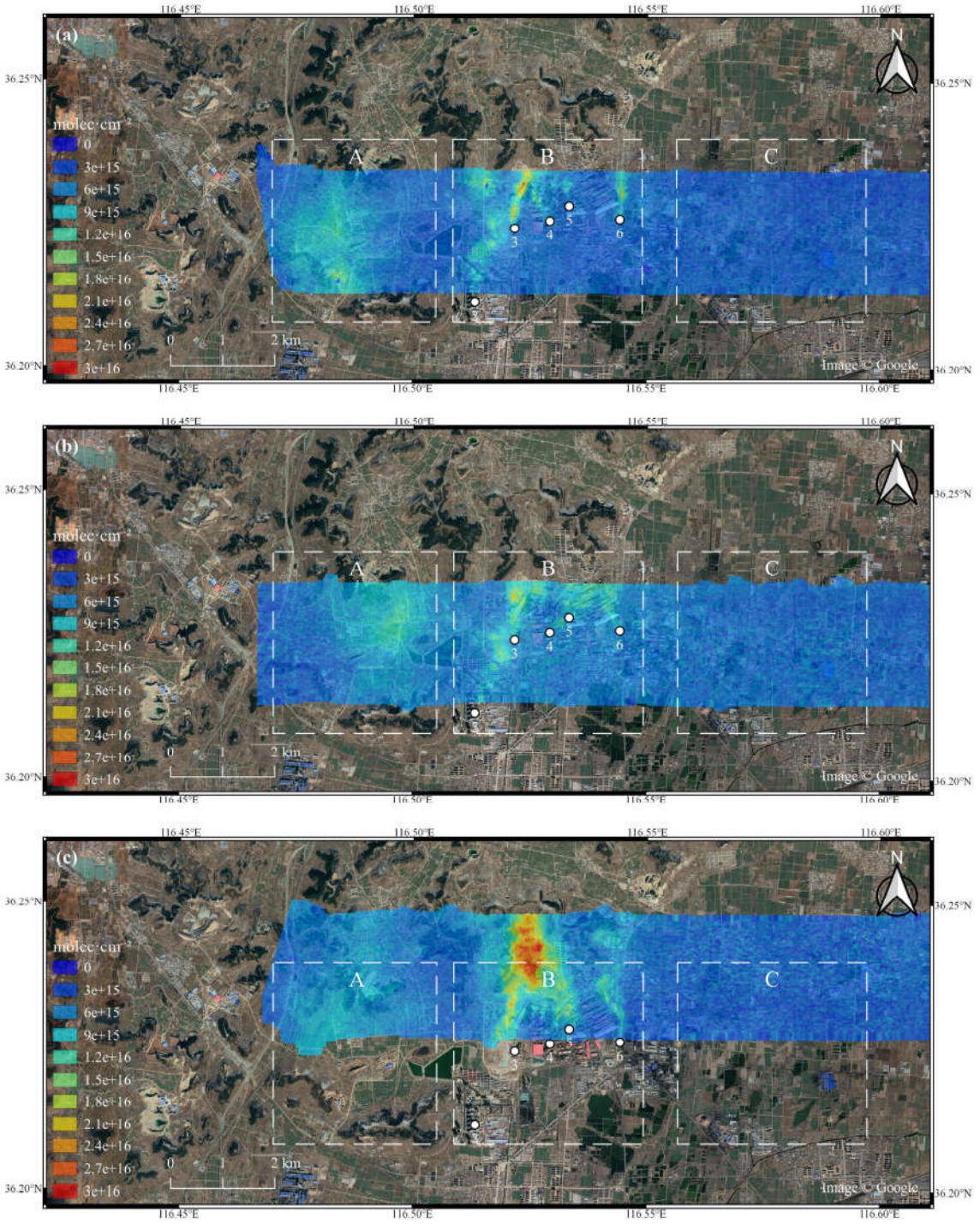

Figure 12. Three flight lines that pass through the steel factory, at local time 13:26 (a), 13:32 (c), and 14:57 (b). Panel (a) and (b) represent flight lines that cover the same area with a 1.5 hour time gap, panel (a) and (c) represent adjacent flight lines with a 6 minutes time gap.

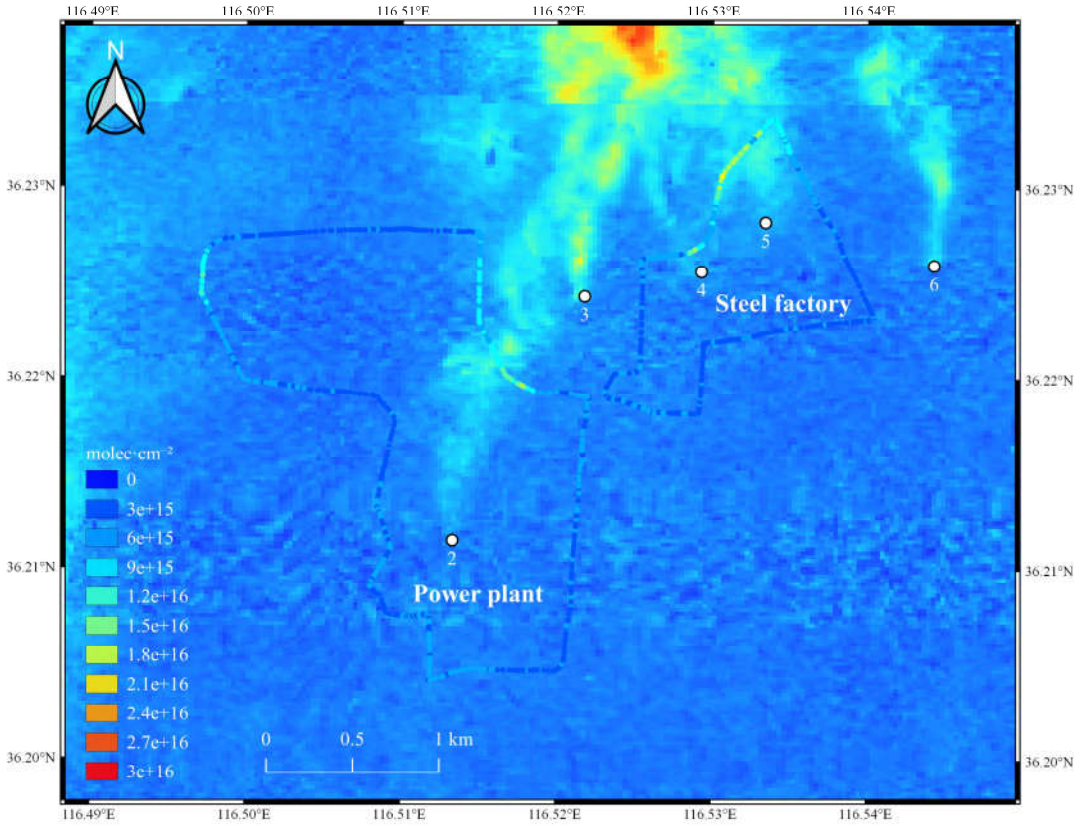

Figure 13. Overview of VCDs retrieved from ground-based mobile DOAS system (circle marks), and VCDs retrieved by UVHIS (background layer), measured on 23 June 2018.

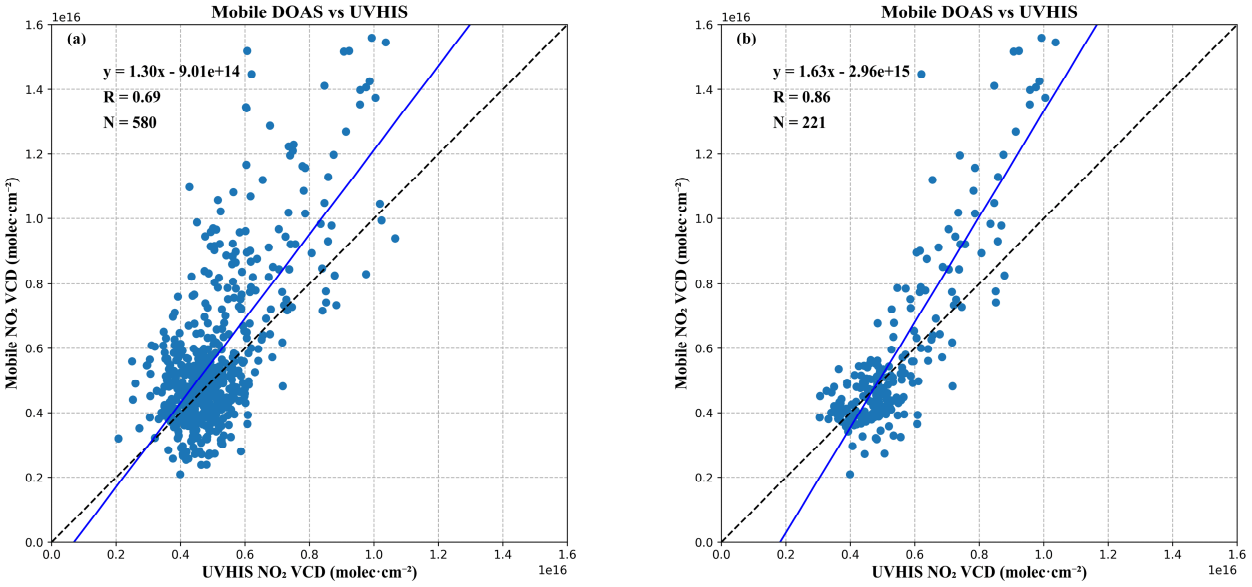

Figure 14. Scatter plot and linear regression analysis of the co-located NO_2 VCDs, retrieved from UVHIS and mobile DOAS system, (a) for all co-located measurements, (b) for co-located measurements that only circled the steel factory.